

**Time-Resolved Resonant Inelastic X-ray Scattering of Graphite
from First Principles**

Masterarbeit

Zur Erlangung des akademischen Grades
Master of Science (M.Sc.)
im Fach Physik

Eingereicht an der
Humboldt-Universität zu Berlin
Mathematisch-Naturwissenschaftliche Fakultät
Institut für Physik

von Elias Richter

Geburtsdatum 25. Dezember 1999
geboren in Berlin
E-Mail richtere@physik.hu-berlin.de

Erstgutachter:in Prof. Dr. Claudia Draxl
Zweitgutachter:in Dr. Francesco Sottile

Abgabetermin 21. Juli 2025

Abstract

Resonant inelastic X-ray scattering (RIXS) is a powerful, state-of-the-art spectroscopic technique that provides access to a range of electronic excitations. Unlike conventional spectroscopies, which typically focus on either valence or core excitations, RIXS captures the interplay between both on a broad energy scale. In this work, we develop a theoretical framework for time- and polarization-resolved RIXS based on an all-electron treatment within the formalism of the Bethe–Salpeter equation (BSE) within many-body perturbation theory (MBPT). Using graphite, a layered van-der-Waals material with anisotropic electronic properties and rich excitation spectra, as a model system, we solve the BSE on top of density-functional theory (DFT) and real-time time-dependent DFT (RT-TDDFT) calculations. We demonstrate the capability of our approach to compute polarization- and angle-resolved RIXS spectra under both equilibrium and optically pumped conditions and investigate the results on their dependence on the photon polarization, reproducing key excitonic features observed in recent experiments.

Zusammenfassung

Resonante inelastische Röntgenstreuung (RIXS) ist eine moderne spektroskopische Methode, mit der sich eine Vielzahl elektronischer Anregungen untersuchen lässt. Im Gegensatz zu konventionellen Ansätzen auf Basis der Bethe-Salpeter-Gleichung (BSE) innerhalb der Vielteilchen-Störungstheorie (MBPT), welche meist entweder Valenz- oder Kernanregungen adressieren, ermöglicht RIXS den Zugang einer Kombination beider, über einen weiten Energiebereich hinweg. In dieser Arbeit präsentieren wir einen theoretischen Ansatz für zeit- und polarisationsaufgelösten RIXS basierend auf dem BSE-Formalismus mit Berücksichtigung aller im System vorhandener Elektronen. Am Beispiel von Graphit, einem geschichteten Van-der-Waals-Material mit anisotropen elektronischen Eigenschaften und komplexem Anregungsspektrum, kombinieren wir Dichtefunktionaltheorie (DFT), zeitabhängige Dichtefunktionaltheorie (RT-TDDFT) und die Lösung der BSE. Wir demonstrieren, dass unser Ansatz die Berechnung polarisations- und winkelabhängiger RIXS-Spektren sowohl im Gleichgewichtszustand, als auch für optisch angeregte Systeme ermöglicht. Dabei analysieren wir insbesondere den Einfluss der Photonenpolarisation und reproduzieren zentrale exzitronische Merkmale, die in aktuellen Experimenten beobachtet wurden.

Contents

1	Introduction	1
2	Theoretical Background	3
2.1	The quantum-mechanical many-body problem	3
2.2	Density Functional Theory	3
2.2.1	Kohn-Sham equations	4
2.2.2	Exchange-correlation functionals	5
2.3	Real-time time-dependent density functional theory	6
2.4	Many-body perturbation theory	7
2.4.1	Bethe-Salpeter equation	7
2.4.2	Quasi-particles	8
2.4.3	Bethe-Salpeter equation as an eigenvalue problem	9
2.4.4	Absorption spectra from BSE	11
2.5	Resonant inelastic X-ray scattering spectroscopy	11
2.5.1	Direct and indirect RIXS	13
2.5.2	RIXS in the independent-particle approximation	13
2.5.3	RIXS in many-body perturbation theory	15
3	Methods	18
3.1	Numerical solution of DFT in exciting	18
3.2	Numerical solution of the BSE eigenvalue problem in exciting	20
3.3	Numerical solution of resonant inelastic X-ray scattering	21
3.3.1	RIXS pathways from BSE in BRIXS	22
3.3.2	Post processing with pyBRIXS	23
3.4	Workflow	23
4	RIXS in graphite	25
4.1	Structural properties of graphite	25
4.2	Experimental work	26
4.3	Electronic structure	26
4.4	Spectroscopy in graphite	28
4.4.1	Optical spectra	28
4.4.2	K -edge spectra	29
4.5	RIXS calculations for graphite	30
4.6	Non-equilibrium spectroscopy in graphite	32
4.7	RIXS for non-equilibrium graphite	34
5	Conclusions and Outlook	37
A	Appendix	39
A.1	2nd Quantization	39
A.2	Derivation of the BSE	39
A.3	Hedin's equations and GW approximation	41
A.4	RIXS in the IPA	42
A.5	RIXS in many-body perturbation theory	43

List of Figures

1	Schema direct RIXS process	13
2	Schema indirect RIXS process	14
3	Schema RIXS process in terms of pathways	17
4	Comparison of BRIXS for χ and $\bar{\chi}$	23
5	Workflow scheme	24
6	Experimental setup	26
7	Band structure and density of states of graphite	27
8	Optical absorption spectra of static graphite	28
9	Optical spectra for static graphite: Literature comparison	29
10	Carbon K-edge core absorption spectra for static graphite for $\alpha = 30, 59^\circ$	29
11	Carbon K-edge RIXS of graphite for incident angles of 30° & 59°	30
12	Carbon K-edge RIXS of graphite for incident angles of 30° & 59° from singlet BSE & IPA	31
13	Optical absorption spectra for non-equilibrium graphite for $\Delta t = 150$ fs	33
14	Carbon K-edge spectra for non-equilibrium graphite for $\Delta t = 150$ fs	33
15	Carbon K-edge RIXS of non-equilibrium graphite for $\Delta t = 150$ fs and incident angles of 30° & 59°	34
16	Differences Carbon K-edge RIXS btw. equilibrium and non-equilibrium graphite for incident angles of 30° & 59° and delay time $\Delta t = 150$ fs	35
17	Carbon K-edge RIXS of non-equilibrium graphite for $\omega_1 = 285.02$ eV & 285.57 eV and incident angles of 30° & 59°	36

1 Introduction

The study of excitation spectra in solids is a central major interest in modern condensed matter physics, ranging from single-particle transitions to collective phenomena. While ground state properties are well captured within the framework of density functional theory (DFT), the description of excited states requires more advanced methods that incorporate particle interactions. Many-body perturbation theory (MBPT) has emerged as the state-of-the-art approach for describing neutral excitations in solids [1]. It provides a systematic framework for computing both optical and X-ray absorption spectra. At the heart of MBPT lies the concept of Green's functions, which describe the propagation of electrons and holes in an interacting system. The Bethe-Salpeter equation (BSE) for the two-particle correlation function, unlike simpler approaches such as the independent-particle approximation (IPA) or the random phase approximation (RPA), captures bound electron-hole states (excitons), enabling an accurate description of excitation spectra [2].

While for BSE-based calculations the focus is on specific energy regions, focusing either on valence or core-level excitations, resonant inelastic X-ray scattering (RIXS) combines both and is integrated within the MBPT framework by Christian Vorwerk [3–5]. In physical terms, RIXS is a 'photon-in photon-out' two-step scattering process, in which an incident X-ray photon excites a core electron to an unoccupied state, followed by radiative decay that emits a photon with reduced energy. The resulting energy loss corresponds to the creation of low-energy excitations in the final state system. Importantly, RIXS provides momentum- and polarization-resolved spectroscopy of a broad spectrum of low-energy excitations [6].

Recent advances in ultrafast X-ray sources have enabled time-resolved RIXS with femtosecond resolution, offering new insights into non-equilibrium electron dynamics. For example, Chen et al. [7] developed a theoretical framework for tr-RIXS based on a non-interacting model, demonstrating how tr-RIXS resolves the momentum- and time-dependent evolution of excitations under optical pumping. These capabilities have opened new directions in understanding transient excitations and electron dynamics in real time, which we aim to extend to the level of MBPT in order to capture excitonic effects under non-equilibrium conditions.

A particularly interesting material in this context is graphite, a layered van-der-Waals solid composed of stacked graphene sheets with practical relevance for optoelectronics and solar energy harvesting [8]. Its electronic structure is characterized by delocalized π -electrons and strong anisotropy between in-plane and out-of-plane directions [9]. Both theory and experiment have confirmed that excitonic effects are strong and must be included for an accurate description of both valence [10, 11] and core level [12, 13] excitation spectra. Due to these properties, graphite serves as a prototypical system for studying excitonic effects.

Early theoretical and experimental work by Carlisle et al. [14, 15] and Shirley et al. [16, 17] have shown that RIXS in graphite is highly sensitive to symmetry selection rules and capable of resolving characteristic features of π - and σ -state excitations, which are already evident at the level of the excitation spectra. Similar excitonic and polarization-resolved RIXS features have also been observed in the closely related two-dimensional material graphene [18], further emphasizing the role of dimensionality and symmetry in carbon-based π -systems. More recently, Dashwood et al. [19] demonstrated that RIXS at the carbon K-edge can even resolve vibronic coupling in σ^* states far above the Fermi level, emphasizing the sensitivity of RIXS to electron-phonon interaction.

Due to the anisotropic structure of graphite, experimental scattering setup, as well as the polarization vectors have a strong influence on the measured spectra and must be

accounted for in the theoretical modeling. This has been confirmed both experimentally [20] and theoretically [21], emphasizing the need to consider these aspects when comparing with experimental results.

In collaborative experimental work by Malvestuto et al. [22], RIXS spectra of graphite were measured under both equilibrium and non-equilibrium conditions. To induce a non-equilibrium state, an additional optical pump pulse was applied, creating a transient redistribution of electronic occupations. Subsequent time- and polarization-resolved RIXS measurements at various pump-probe delay times revealed pronounced modifications in the spectra, attributed to both changes in the electronic occupation and the modification of excitonic modes.

In this thesis, we present a theoretical framework for polarization-sensitive time-dependent RIXS, based on the Bethe-Salpeter equation and apply it to optically pumped and unpumped carbon K-edge RIXS in graphite. Starting either from ground state DFT or from non-equilibrium electron distributions obtained via real-time time-dependent DFT (RT-TDDFT) simulations of the pump process, we compute both valence and core-level absorption spectra by numerically solving the BSE. Based on these calculations, we calculate time-resolved RIXS spectra for different experimental setups. By incorporating both incoming and outgoing light polarization vectors, our model also accounts for the polarization dependence, enabling direct comparison with experiments and capturing the essential features of the experimental setups. We provide a comprehensive analysis of both excitation and RIXS spectra in terms of the underlying electronic structure and excitonic effects.

2 Theoretical Background

This chapter introduces the theoretical foundations used in this work. Starting from the quantum-mechanical many-body problem, it begins with a brief review of density function theory (DFT) and real-time time-dependent DFT (RT-TDDFT) for ground-state and time-dependent phenomena. Subsequently, the focus shifts to many-body perturbation theory (MBPT), in particular the Bethe-Salpeter equation (BSE), as a tool to account for quasi-particle and excitonic effects. Finally, the formalism of resonant inelastic X-ray scattering (RIXS) is presented in detail, starting from the independent particle approximation and extending to a many-body framework, analyzing the role of excitonic effects.

2.1 The quantum-mechanical many-body problem

Predicting the properties of a material is the fundamental task of theoretical solid-state physics and can be achieved by solving the time-dependent Schrödinger equation for a many-body system of interacting particles,

$$i\frac{\partial}{\partial t}\Psi(\{\mathbf{r}_i\}, \{\mathbf{R}_I\}; t) = \hat{H}\Psi(\{\mathbf{r}_i\}, \{\mathbf{R}_I\}; t), \quad (2.1)$$

where Ψ is the full many-body wavefunction, and \hat{H} is the many-body Hamiltonian. For a system consisting of M nuclei and N electrons, the non relativistic Hamiltonian is given by

$$\hat{H} = -\frac{1}{2}\sum_i^N \nabla_i^2 - \sum_i^N \sum_I^M \frac{Z_I}{|\mathbf{r}_i - \mathbf{R}_I|} + \frac{1}{2}\sum_{i \neq j}^N \frac{1}{|\mathbf{r}_i - \mathbf{r}_j|} - \sum_I^M \frac{1}{2M_I} \nabla_I^2 + \frac{1}{2}\sum_{I \neq J}^M \frac{Z_I Z_J}{|\mathbf{R}_I - \mathbf{R}_J|}. \quad (2.2)$$

Here, \mathbf{R}_I , Z_I , and M_I denote the coordinates, the atomic number, and the mass of the I -th atom, respectively, while \mathbf{r}_i is the coordinate of the i -th electron. Atomic units are used throughout this thesis, meaning $\hbar = m_e = 4\pi\epsilon_0^{-1} = 1$.

Despite its compact form, solving the $M + N$ -particle Schrödinger equation directly is not feasible for any realistic system [23]. The Coulomb interaction results in a high-dimensional system of coupled differential equations, making an exact solution computationally prohibitive. A widely used approach and first step to reduce this complexity, is the Born-Oppenheimer approximation [24]. Given the large mass difference between electrons and atomic nuclei, their motion can be decoupled. This allows for fixing the positions of the nuclei and solve the electronic Schrödinger equation. For a system of N electrons, the electronic Hamiltonian is given by

$$\hat{H}_e = -\frac{1}{2}\sum_i^N \nabla_i^2 - \sum_i^N \sum_I^M \frac{Z_I}{|\mathbf{r}_i - \mathbf{R}_I|} + \frac{1}{2}\sum_{i \neq j}^N \frac{1}{|\mathbf{r}_i - \mathbf{r}_j|}. \quad (2.3)$$

2.2 Density Functional Theory

Nonetheless, even the numerical solution of the decoupled electronic system remains computationally intractable for most systems. In order to approach the ground state properties, the many-electron problem is typically reformulated within the the framework of density-functional theory (DFT) by describing the system in terms of the electronic density rather than the many-electron wave function. While the full complexity of the system is retained in an unknown universal density functional $F[n]$, this formulation allows the search for the ground-state properties in a simplified way. According to the Hohenberg-Kohn theorem [25], all ground-state observables of an interacting electron system can, in principle, be expressed as functionals of the ground-state density. Therefore it provides the mathematical

foundation for describing the ground state of a many-electron system solely in terms of the electron density.

The theorem establishes the existence of the total energy functional $E[n]$. The most general expression for it is given by

$$E[n] = F[n] + \int d^3r n(\mathbf{r}) v_{\text{ext}}(\mathbf{r}), \quad (2.4)$$

where the universal, system independent, density functional $F[n]$ includes the kinetic energy and two-particle interaction of the system. It states that, for any system of interacting electrons in an external potential, there is a one-to-one correspondence, up to an arbitrary additive constant, between the external potential v_{ext} and ground-state electron density $n_0(\mathbf{r})$. Consequently, every ground state property of the system can be expressed as a functional of the ground state density alone. Applying the variational principle to the functional $E[n]$, yields the ground-state energy E_0 and density $n_0(\mathbf{r})$:

$$E_0 = E[n_0(\mathbf{r})] = \min_{n(\mathbf{r})} E[n(\mathbf{r})]. \quad (2.5)$$

A proof of the Hohenberg-Kohn theorem can be found in [26].

2.2.1 Kohn-Sham equations

While the Hohenberg-Kohn theorems ensure that all ground-state properties are determined by the ground-state density, the explicit form of the universal functional $F[n]$ remains unknown. Consequently, a central challenge of DFT is to find a practical way to determine the ground-state density without knowing the exact functional. To circumvent this issue, Kohn and Sham proposed in 1965 a practical scheme to find the ground-state density of an interacting system [27]. Their approach is based on the idea of replacing the original interacting many-electron system with an auxiliary system of fictitious non-interacting particles that yield the same ground-state density as the real system. The energy functional for these non-interacting particles is formulated as

$$E_{\text{KS}}[n] = T_S[n] + \int d^3r n(\mathbf{r}) v_{\text{ext}}(\mathbf{r}) + E_H[n] + E_{xc}[n], \quad (2.6)$$

where T_S is the kinetic energy of the non-interacting system, E_H is the electrostatic Hartree energy, defined as

$$E_H[n] = \frac{1}{2} \int d^3r \int d^3r' \frac{n(\mathbf{r})n(\mathbf{r}')}{|\mathbf{r} - \mathbf{r}'|}, \quad (2.7)$$

and E_{xc} the exchange-correlation energy functional. The latter determines the equality of the total energy in Eq. (2.4) and (2.6). It contains the difference between the kinetic energy and T_S , as well as between the true electron-electron interaction and the Hartree energy. However, the exact form of E_{xc} is unknown and must be approximated in practice.

The ground-state density is obtained by minimizing the energy functional under the constraint of particle number conservation. This leads to

$$\int d^3r \left(\frac{\delta T_S[n]}{\delta n(\mathbf{r})} + v_{\text{KS}}(\mathbf{r}) - \mu \right) \delta n(\mathbf{r}) = 0, \quad (2.8)$$

where μ is the Lagrange multiplier associated with the conservation of the total number of electrons. Here, the Kohn-Sham effective potential v_{KS} is given by

$$v_{\text{KS}}(\mathbf{r}) = v_{\text{ext}}(\mathbf{r}) + v_H(\mathbf{r}) + v_{xc}(\mathbf{r}), \quad (2.9)$$

where v_H is the Hartree potential and v_{xc} the exchange-correlation potential are defined as

$$v_H(\mathbf{r}) = \frac{\delta E_H[n]}{\delta n(\mathbf{r})} = \int d^3r' \frac{n(\mathbf{r}')}{|\mathbf{r} - \mathbf{r}'|}, \quad \text{and} \quad v_{xc}(\mathbf{r}) = \frac{\delta E_{xc}[n]}{\delta n(\mathbf{r})}. \quad (2.10)$$

Kohn and Sham proposed that the same equation as in Eq. (2.8) could be formulated for a system of fictitious non-interacting particles in an effective potential, v_{KS} . Consequently, they deduced that the ground state density of the interacting system can be acquired by solving a set of single-particle Schrödinger equations for a non-interacting system described by

$$\left[-\frac{1}{2}\nabla^2 + v_{KS}(\mathbf{r}) \right] \psi_{n\mathbf{k}}^{KS}(\mathbf{r}) = \epsilon_{n\mathbf{k}}^{KS} \psi_{n\mathbf{k}}^{KS}(\mathbf{r}), \quad (2.11)$$

such that the ground-state density of the interacting system is given by the sum over all occupied single particle states as

$$n_0(\mathbf{r}) = \sum_{n\mathbf{k}} |\psi_{n\mathbf{k}}^{KS}(\mathbf{r})|^2. \quad (2.12)$$

Equations (2.11) and (2.12), together with the definition of v_{KS} , constitute the Kohn-Sham equations. These equations are formally exact. In practice, however, they need to be solved self-consistently for the ground state density, starting from an initial guess for $n_0(\mathbf{r})$. Despite relying on an unknown exchange-correlation functional, this approach enables practical calculations of ground-state properties with remarkable accuracy and has become the foundation of modern electronic structure theory.

2.2.2 Exchange-correlation functionals

Since all many-body effects of the interacting system are contained in the xc functional, and neither the exact difference in kinetic energy nor the exchange and correlation contributions beyond the classical Hartree term are known, approximations must be employed. While the exact xc potential would provide the exact ground-state properties, the accuracy of DFT fundamentally depends on the level of approximation. The concept of "Jacob's Ladder" [28], introduced by Perdew, categorizes different levels of approximations based on their accuracy and complexity. While the bottom bellow the ladder corresponds to the Hartree approximation and is considered as "hell", the desired top level is delineated as "chemical heaven", which often is beyond current practical capabilities. Climbing higher on the ladder typically leads to improved accuracy but also entails a substantial increase in computational cost.

A simple approximation and first rung of the ladder is given by the local density approximation (LDA), where the exchange-correlation energy depends locally on the density only. The exchange energy per atom is given by the corresponding exchange energy of the homogeneous electron gas with density n . LDA is primarily valid for systems with slowly-varying densities. Despite its limitations, it remains widely used and successful in many applications.

However, to improve accuracy in systems with more complex densities more sophisticated approximations were developed. An extension of LDA is given by the generalized gradient approximation (GGA), where the exchange-correlation functional is described by

$$E_{xc}^{GGA}[n] = \int d^3r n(\mathbf{r}) \epsilon_{xc}(n(\mathbf{r}), \nabla n(\mathbf{r})). \quad (2.13)$$

The most popular and best-known GGA functional is the PBE functional, developed by Perdew, Burke, and Ernzerhof [29]. Another well known GGA functional is PBEsol [30],

which is optimized for solids. In this work, we will exclusively use the PBE functional, since an important feature, the van der Waals correction, is optimized for that. However, while GGA functionals are widely used and yield reliable results, they also exhibit well-documented limitations. PBE tends to overestimate lattice constants and underestimate band gaps. In addition, it is known to provide less accurate descriptions of strongly correlated systems and magnetic properties [31, 32]. More advanced functionals, such as meta-GGA [33] and hybrid functionals [34], offer improved accuracy, but at the cost of significantly higher computational expense.

2.3 Real-time time-dependent density functional theory

While the Kohn-Sham approach, following the Hohenberg-Kohn theorems, is valid for static systems, in practice, theoretical spectroscopy often aims to describe electronic systems under the influence of time-dependent external potentials, such as ultrafast laser excitations. Time-dependent Density-Functional Theory (TDDFT), as a time dependent extension of the DFT, provides the theoretical framework for describing these effects, enabling the study of non-equilibrium electron dynamics [35]. Analogous to the Hohenberg-Kohn theorem for the static case, the Runge-Gross theorem establishes that there is a one-to-one correspondence between the external potential $v_{\text{ext}}(\mathbf{r}, t)$ and the time-dependent density $n(\mathbf{r}, t)$ at time t [36], thereby making the density the basic variable also in the time-dependent setting. However, TDDFT has a limited time scale, since beyond a certain point approximations such as the adiabatic approximation do not state anymore.

Due to the Runge-Gross theorem, a time-dependent Kohn-Sham scheme can be formulated by introducing an auxiliary system of non-interacting electrons in an external potential v_{KS} , satisfying the time-dependent Schrödinger equation

$$i \frac{\partial}{\partial T} \psi_i^{\text{KS}}(\mathbf{r}, t) = \left[-\frac{\nabla^2}{2} + v_{\text{KS}}[n](\mathbf{r}, t) \right] \psi_i^{\text{KS}}(\mathbf{r}, t) = \hat{H}^{\text{KS}} \psi_i^{\text{KS}}(\mathbf{r}, t). \quad (2.14)$$

As for the ground state, the time-dependent Kohn-Sham potential is given by

$$v_{\text{KS}}(\mathbf{r}, t) = v_{\text{ext}}(\mathbf{r}, t) + v_H(\mathbf{r}, t) + v_{xc}(\mathbf{r}, t). \quad (2.15)$$

The third term v_{xc} contains all non-trivial many body interactions, requiring approximations similar to those in the static case. Further details can be found in [1, 37].

In practice, TDDFT problems are either approached in the linear response framework, by evaluating the density as a first-order response to an external perturbation, or in the real-time domain, by directly evolving the Kohn-Sham wavefunctions [38]. Here, we want to focus on the framework of real-time time-dependent density functional theory (RT-TDDFT) in order to study pump-probe spectroscopy and the coherent excitation dynamics.

Starting from a ground-state calculation, we consider a time-dependent KS Hamiltonian with an additional perturbation in terms of an external electric field $\mathbf{E}(t)$ given by

$$\hat{H}(\mathbf{r}, t) = \frac{1}{2} \left(-i\nabla + \frac{1}{c} \mathbf{A}(t) \right)^2 + v_{\text{KS}}(\mathbf{r}, t), \quad (2.16)$$

where $\mathbf{A}(t)$ is the vector potential connected to $\mathbf{E}(t)$, and c is the speed of light. The time evolved Kohn-Sham wavefunctions are expressed by

$$|\psi_{j\mathbf{k}}\rangle(t + \Delta t) = \hat{U}(t + \Delta t, t) |\psi_{j\mathbf{k}}\rangle(t) \quad (2.17)$$

with the propagator given by

$$\hat{U}(t + \Delta t, t) = \hat{T} \left[\exp \left(-i \int_t^{t+\Delta t} d\tau \hat{H}(\tau) \right) \right]. \quad (2.18)$$

\hat{T} is the time-ordering operator. Different propagators such as a simple exponential, approximate enforced time-reversal symmetry, or Runge-Kutta of 4th order can be employed [39].

In order to perform calculations that include electron-hole interactions, for a non-equilibrium system, the main quantities of interest are the occupation numbers. Within RT-TDDFT, for a given \mathbf{k} -point, the number of electrons excited to an unoccupied KS state j is described by

$$m_{j\mathbf{k}}^e(t) = \sum_i f_{i\mathbf{k}} |\langle \psi_{j\mathbf{k}}(0) | \psi_{i\mathbf{k}}(t) \rangle|^2. \quad (2.19)$$

Similarly, the number of holes created in an occupied KS state is given by

$$m_{j'\mathbf{k}}^h(t) = f_{j'\mathbf{k}} - \sum_i f_{i\mathbf{k}} |\langle \psi_{j'\mathbf{k}}(0) | \psi_{i\mathbf{k}}(t) \rangle|^2. \quad (2.20)$$

The total time-dependent electronic density is

$$n(\mathbf{r}, t) = \sum_{j\mathbf{k}} w_{\mathbf{k}} f_{j\mathbf{k}} |\psi_{j\mathbf{k}}(\mathbf{r}, t)|^2, \quad (2.21)$$

with $w_{\mathbf{k}}$ being the weight of the \mathbf{k} -point.

2.4 Many-body perturbation theory

As described in the previous sections, DFT allows for the simplification of the many-body problem by formulating the total energy as a functional of the electron density and minimizing with respect to it. However, when studying excited-state properties of the system, e.g., spectroscopic observables, the interpretation of the KS eigenstates as non-interacting particles is not adequate. An alternative theoretical framework is provided by many-body perturbation theory (MBPT). This framework builds on field-theoretical concepts and allows for a more rigorous treatment of electron-electron interaction. It is convenient to describe the many-body Hamiltonian in terms of fermionic field operators using the second quantization formalism and adopt the occupation number representation. Additional information is provided in the Appendix A.1, where we follow the derivations presented in Refs. [23, 40, 41].

2.4.1 Bethe-Salpeter equation

At the heart of MBPT lies the concept of the time-ordered one-particle Green's function [42]

$$G(\mathbf{r}_1, t_1; \mathbf{r}_2, t_2) = G(1, 2) = -i \langle 0 | \hat{T} [\hat{\psi}(1) \hat{\psi}^\dagger(2)] | 0 \rangle, \quad (2.22)$$

which can be interpreted as a measure for the probability of a particle propagation from position \mathbf{r}_1 at time t_1 to position \mathbf{r}_2 at time t_2 . All possible interaction are included within the Green's function. Here the short notation $(1) = (\mathbf{r}_1, t_1)$ is used. $\hat{\psi}$ and $\hat{\psi}^\dagger$ are the field annihilation and creation operators in the Heisenberg picture.

The corresponding time-ordered two-particle Green's function describes the correlated propagation of two particles and is defined as

$$G(1, 2; 1', 2') = (-i)^2 \langle 0 | \hat{T} [\hat{\psi}(1) \hat{\psi}(2) \hat{\psi}^\dagger(2') \hat{\psi}^\dagger(1')] | 0 \rangle. \quad (2.23)$$

The Heisenberg equations of motion for the one-particle Green's function reads [43]

$$\left[i \frac{\partial}{\partial t_1} - h(\mathbf{r}_1) \right] G(1, 1') + i \int d^3 r_2 v_c(\mathbf{r}_1, \mathbf{r}_2) G_2(1, 2; 1', 2^+) \Big|_{t_2=t_1^+} = \delta(1, 1'), \quad (2.24)$$

where $t^+ = t + \delta t$ ensures proper time ordering. Note that the two-particle Green's function G_2 appears in the equation of motion due to the two-particle interaction in v_c . Analogously, the three-particle Green's function enters the equation for G_2 . In general, determining the n -particle Green's function G_n requires knowledge on the Green's functions G_{n-1} and G_{n+1} . The constructed set of equations is called Martin-Schwinger hierarchy [23, 43].

The two-particle correlation function L is introduced as

$$L(1, 2, 1', 2') = -G_2(1, 2, 1', 2') + G(1, 1')G(2, 2'), \quad (2.25)$$

satisfying a Dyson equation

$$L(1, 2, 1', 2') = L_0(1, 2, 1', 2') + L_0(1, \bar{3}', 1', \bar{3}') \Xi(\bar{3}, \bar{4}, \bar{3}', \bar{4}') L(\bar{4}', 2, \bar{4}, 2'), \quad (2.26)$$

with

$$L_0(1, 2, 1', 2') = G(1, 2')G(2, 1') \quad (2.27)$$

and the two-particle interaction kernel Ξ . This equation is known as the Bethe-Salpeter equation (BSE) [40, 44]. Additional derivations can be found in Appendix A.2 following the derivations in [23].

Also related to the correlation function L is the full (reducible) polarizability χ given by

$$\chi(1, 2) = -i \frac{G(1, 1^+)}{\delta v(2^+, 2)} = -i L(1, 2, 1^+, 2^+). \quad (2.28)$$

The BSE can be derived from Hedin's equations via functional differentiation of the Green's function with respect to the external potential. Further approximations are provided by the GW approach. The connection is outlined in Appendix A.3. Still, although the BSE formally follows from Hedin's equations, in practice, it is often applied on top of DFT calculations, using DFT eigenstates and an approximate statically screened kernel.

2.4.2 Quasi-particles

One of the main concepts of applying MBPT is to replace the many-body system of N strongly interacting particles by a system of non-interacting or weakly interacting quasi-particles. These quasi-particles are not real particles, but effective states that incorporate many-body interactions. However, properties such as mass, charge, and momentum change are normalized by the influence of all other electrons in the system.

The theoretical foundation for the description of quasi-particles is the single-particle Green's function formalism. In particular, the quasi-particle wavefunctions $\psi_{i\mathbf{k}}^{QP}$ and energies $\epsilon_{i\mathbf{k}}^{QP}$ are obtained as solutions of the quasi-particle Schrödinger equation

$$\hat{h}(\mathbf{r}) \psi_{i\mathbf{k}}^{QP}(\mathbf{r}) + \int d^3 r' \Sigma(\mathbf{r}, \mathbf{r}', \epsilon_{i\mathbf{k}}^{QP}) \psi_{i\mathbf{k}}^{QP}(\mathbf{r}') = \epsilon_{i\mathbf{k}}^{QP} \psi_{i\mathbf{k}}^{QP}(\mathbf{r}), \quad (2.29)$$

where $\hat{h}(\mathbf{r})$ is the mean-field Hamiltonian (e.g., Kohn-Sham or Hartree-Fock). Within the quasi-particle approximation, the Dyson equation for $G(1, 2)$ in (A.23) can be approximately solved, leading to the spectral representation

$$G(\mathbf{r}_1, \mathbf{r}_2; \omega) = \sum_{i\mathbf{k}} \frac{\psi_{i\mathbf{k}}^{QP}(\mathbf{r}_1) \left[\psi_{i\mathbf{k}}^{QP}(\mathbf{r}_2) \right]^*}{\omega - \epsilon_{i\mathbf{k}}^{QP} - i\eta}, \quad (2.30)$$

where the poles of G directly correspond to the energies of quasi-particle excitations. This expression explicitly shows that the Green's function describes the propagation of single-particle excitations in terms of quasi-particle states and their associated energies [40].

A closely related concept applies to excitons, i.e., bound electron-hole pairs. These can be described as correlated two-particle excitations and are formally obtained from the two-particle Green's function. In analogy to the quasi-particle picture, excitonic states appear as poles of this two-particle Green's function, and their energies can be extracted by solving a reformulated eigenvalue problem of the BSE. In its matrix form, the eigenvalues of the Hamiltonian correspond to exciton energies, and the eigenvectors describe the excitonic wavefunctions. Therefore, the BSE provides a systematic framework to describe electron–electron and electron–hole interactions, respectively.

Thus, both quasi-particles and excitons are accessible via Green's function methods, and both lead to an eigenvalue formulation that captures the essence of the many-body excitation spectrum.

2.4.3 Bethe-Salpeter equation as an eigenvalue problem

So far, we have discussed the BSE only in its complex integral formulation, as given in Eq.(2.27). However, it can also be cast into a more accessible and numerically tractable form by expressing it in matrix notation, where all functions are expanded in terms of a two-particle basis. The quasi-particle states can be separated into occupied (o) and unoccupied (u) states. Following the approach of Rohlfing and Louie [2], as well as the derivations by Puschnig [45] and Sagmeister [46], the BSE can be formulated as an eigenvalue problem

$$\sum_{o'u'\mathbf{k}'} H_{o\mathbf{k},o'u'\mathbf{k}'}^{\text{BSE}} A_{o'u'\mathbf{k}'}^\lambda = E^\lambda A_{o'u'\mathbf{k}'}^\lambda, \quad (2.31)$$

where \mathbf{k} indicates points in the reciprocal space, $A_{o\mathbf{k}}^\lambda$ is the excitonic eigenvector, and E^λ is the corresponding exciton energy.

The exciton wave-function in the two-particle basis is given by

$$\psi^\lambda(\mathbf{r}_h, \mathbf{r}_e) = \sum_{u\mathbf{k}} A_{o'u'\mathbf{k}'}^\lambda \phi_{o\mathbf{k}}^*(\mathbf{r}_h) \phi_{u\mathbf{k}}(\mathbf{r}_e), \quad (2.32)$$

where \mathbf{r}_e and \mathbf{r}_h denote the electron and hole positions, respectively. The functions $\phi_{i\mathbf{k}}(\mathbf{r})$ are single-particle wavefunctions, typically taken from DFT calculations, i.e., Kohn-Sham wavefunctions. The full BSE Hamiltonian H^{BSE} has a block structure that includes resonant and anti-resonant terms. The resonant block describes excitations from valence to conduction bands (i.e., absorption), while the anti-resonant block corresponds to de-excitations (i.e., emission). To reduce computational complexity, the Tamm-Dancoff approximation (TDA) is often employed. It neglects the coupling between resonant and anti-resonant components, i.e., positive and negative frequencies ω , effectively reducing the problem to the resonant block only [47]. Under this approximation, the BSE Hamiltonian decomposes into three additive contributions as

$$H^{\text{BSE}} = H^{\text{diag}} + 2\gamma_x H^x + \gamma_c H^c. \quad (2.33)$$

Here, the factors γ_x and γ_c allow to select different levels of approximation. The term H^{diag} describes the diagonal component, given by

$$H_{o\mathbf{k},o'u'\mathbf{k}'}^{\text{diag}} = (\epsilon_{u\mathbf{k}} - \epsilon_{o\mathbf{k}}) \delta_{oo'} \delta_{uu'} \delta_{\mathbf{k},\mathbf{k}'}, \quad (2.34)$$

where $\epsilon_{n\mathbf{k}}$ denotes the single-particle energy of orbital n at wavevector \mathbf{k} , typically obtained from DFT or GW .

Retaining only this term (i.e., $\gamma_x = \gamma_c = 0$) corresponds to the independent particle approximation. The exchange term H^x , which describes repulsive interactions, is defined by

$$H_{ouk,o'u'k'}^x = \iint d^3r d^3r' \phi_{ok}(\mathbf{r}) \phi_{uk}^*(\mathbf{r}) \bar{v}_c(\mathbf{r}, \mathbf{r}') \phi_{o'k'}^*(\mathbf{r}') \phi_{u'k'}(\mathbf{r}'), \quad (2.35)$$

caused by the bare coulomb interaction \bar{v}_c , again excluding long-range terms.

Finally, the direct term H^c accounts for the attractive particle-hole correlation between particle and hole via the screened Coulomb interaction w , defined by

$$H_{ouk,o'u'k'}^c = - \iint d^3r d^3r' \phi_{ok}(\mathbf{r}) \phi_{uk}^*(\mathbf{r}') w(\mathbf{r}, \mathbf{r}') \phi_{o'k'}^*(\mathbf{r}') \phi_{u'k'}(\mathbf{r}'). \quad (2.36)$$

The values of the parameters γ_x and γ_c account for the spin degree of freedom and different level of approximation. For instance, neglecting the correlation part (i.e., $\gamma_c = 0$) yields the random phase approximation (RPA) including local field effects. Different spin channels can be accessed via the spin-singlet ($\gamma_x = \gamma_c = 1$) and spin-triplet ($\gamma_x = 0, \gamma_c = 1$) channels. In the latter, the exchange interaction vanishes due to dipole selection rules. For absorption spectroscopy and comparison to experiments, the spin-singlet and thus the full BSE-Hamiltonian is typically used.

Solving the eigenvalue problem in (2.31) yields the correlation function as

$$L_{ouk,o'u'k'} = i \sum_{\lambda} \frac{[A_{ouk}^{\lambda}]^* A_{o'u'k'}^{\lambda}}{\omega - E^{\lambda}}, \quad (2.37)$$

which connects to the polarizability via Eq. (2.28) and subsequently to the macroscopic dielectric function through Eq. (2.42). Both are expressed in the transition space, where the basis states are electron-hole pairs labeled by occupied and unoccupied band indices and crystal momentum, i.e., (o, u, k) with o denoting an occupied (valence) state and u an unoccupied (conduction) state.

The imaginary part of the macroscopic dielectric function, which determines the absorption spectrum, is then given by

$$\text{Im } \epsilon_M^i(\omega) = \frac{8\pi^2}{V} \sum_{\lambda} |\mathbf{t}_{\lambda}^i|^2 \delta(\omega - E^{\lambda}), \quad (2.38)$$

where V denotes the crystal volume, i the polarization and \mathbf{t}_{λ}^i the transition coefficient defined by

$$\mathbf{t}_{\lambda}^i = \sum_{ouk} A_{ouk}^{\lambda} \frac{\langle o\mathbf{k} | \hat{\mathbf{p}} | u\mathbf{k} \rangle}{\epsilon_{uk}^{\text{QP}} - \epsilon_{ok}^{\text{QP}}}, \quad (2.39)$$

with $\hat{\mathbf{p}}$ being the momentum operator and $\mathbf{P}_{ouk} = \langle o\mathbf{k} | -i\nabla | u\mathbf{k} \rangle$ denoting the momentum matrix elements between the respective states o and u .

The physical meaning behind this is the following: The eigenvalue E^{λ} provides the actual excitation energy of the exciton λ , while the corresponding eigenvector A_{ouk}^{λ} describes the composition of the excitation and serves as a weighting factor in the transition coefficients. Thus, detailed information about the exciton is contained in the exciton weights

$$w_{ok}^{\lambda} = \sum_u |A_{ouk}^{\lambda}|^2, \quad \text{and} \quad w_{uk}^{\lambda} = \sum_o |A_{ouk}^{\lambda}|^2, \quad (2.40)$$

which provide inside into the character of the exciton and its contribution to a specific electron transition.

2.4.4 Absorption spectra from BSE

In order to deal with results obtained from the solution of the Bethe-Salpeter Equation, we want to clarify the connection between theoretical concepts and experimental quantities. In optical- or X-ray absorption experiments, one is interested in the average response of a macroscopic system to an electromagnetic perturbation. The absorption spectra is obtained by measuring the transmitted light after irradiating a sample with light of a known wavelength. The measured absorption spectrum is given by the imaginary part of the macroscopic dielectric function ϵ_M , which is related to the microscopic dielectric function ϵ but also, through Hedin's equations, to the correlation function L introduced in the BSE. Adler and Wiser [48, 49] showed that both dielectric functions are connected via

$$\epsilon_M(\omega) = \frac{1}{\epsilon_{\mathbf{G}=0, \mathbf{G}'=0}^{-1}(\mathbf{q}, \omega)} = \frac{1}{1 + v_c(\mathbf{q} + \mathbf{G})\chi_{\mathbf{G}=\mathbf{G}'}(\mathbf{q}, \omega)}. \quad (2.41)$$

Here, $\epsilon_{\mathbf{G}, \mathbf{G}'}(\mathbf{q}, \omega) = \epsilon(\mathbf{q} + \mathbf{G}, \mathbf{q} + \mathbf{G}', \omega)$ denotes the Fourier transform of the dielectric function $\epsilon(\mathbf{r}, \mathbf{r}', t - t')$ into reciprocal space and frequency domain, where \mathbf{q} lies within the first Brillouin zone, and \mathbf{G} is a reciprocal lattice vector. Since the macroscopic dielectric function depends on the inverse dielectric tensor, all components, even with $\mathbf{G}, \mathbf{G}' \neq 0$, contribute. This effect is referred to as local-field effects. It is a consequence of the Dyson equation governing the polarizability and describes induced screening effects in the solid.

For the optical absorption, the wavelength of the perturbation is large compared to the unit cell, corresponding to a small \mathbf{q} , and thus the momentum-dependence can be neglected. For X-rays, this is not strictly fulfilled, but also in this case, the momentum is typically ignored. The proper expression of the macroscopic dielectric function is given by

$$\epsilon_M(\mathbf{q}, \omega) = 1 - \lim_{\mathbf{q} \rightarrow 0} v_c(\mathbf{q})\bar{\chi}_{\mathbf{G}=0, \mathbf{G}'=0}(\mathbf{q}, \omega), \quad (2.42)$$

where $\bar{\chi}$ is a modified polarizability, excluding long-range terms inside the Coulomb interaction v_c , determined by the relation $\bar{\chi} = \chi + \chi \bar{v}_c \bar{\chi}$ [23, 41]. Thus, ϵ_M can be obtained from the results for the correlation function L as computed in a BSE calculation following Eq. (2.28) and the optical absorption spectrum is finally given by $\text{Im} \epsilon_M$.

2.5 Resonant inelastic X-ray scattering spectroscopy

The inelastic scattering of X-rays on condensed matter is a powerful tool for probing the electronic structure and excitations of a material. In an X-ray scattering experiment, a collimated beam of monochromatic X-rays is directed at a sample, and the scattered beam is recorded within a specific solid angle Ω , the region of space in which the detector operates. Information about the spatial structure is obtained by analyzing the scattered particles with respect to the angle, which corresponds to the change in momentum. A general measure for the scattering intensity is given by the differential cross section $d\sigma/d\Omega$. The dynamics of the system can be analyzed by also considering the energy transfer. A measure for the inelastically scattered particles is the double differential cross-section (DDCS) $d^2\sigma/d\Omega dE$, which describes the probability of the scattering into the infinitesimal angle element $d\Omega$ within the infinitesimal energy range dE . Typically, the DDCS is measured as a function of momentum transfer \mathbf{q} and energy loss ω .

From a quantum mechanical perspective, the double differential cross-section characterizes the scattering process in a many-body system and describes transitions from an initial ground state $|i\rangle$ with energy E_i to an excited final state $|f\rangle$ with energy E_f . Following the derivation of [50] and the initial idea of Kramers and Heisenberg [51], the scattering of a photon with energy ω_1 , polarization \mathbf{e}_1 , and momentum \mathbf{K}_1 into a photon with energy

ω_2 , polarization \mathbf{e}_2 , and momentum \mathbf{K}_2 is given by the generalized Kramers-Heisenberg formula [52]

$$\begin{aligned} \frac{d^2\sigma}{d\Omega_2 d\omega_2} = & \alpha^4 \left(\frac{\omega_2}{\omega_1} \right) \sum_f \left| \langle f | \mathbf{e}_1 \cdot \mathbf{e}_2^* \sum_j e^{i(\mathbf{K}_1 - \mathbf{K}_2) \mathbf{r}_j} | i \rangle \right. \\ & \left. + \sum_n \frac{\langle f | \sum_j e^{-i\mathbf{K}_2 \mathbf{r}_j} \mathbf{e}_2^* \cdot \mathbf{p}_j | n \rangle \langle n | e^{i\mathbf{K}_1 \mathbf{r}_j} \mathbf{e}_1 \cdot \mathbf{p}_j | 0 \rangle}{\omega_1 - E_n} \right|^2 \delta(E_f - E_i + \omega_2 - \omega_1), \end{aligned} \quad (2.43)$$

describing the interaction of an incoming photon with the electronic system within second-order perturbation theory. Here $|i\rangle$ and $|f\rangle$ describe the initial and excited final state, respectively. The delta function, containing the energies of initial and final state as well as the photon energies, enforces energy conservation for the entire process. Furthermore, before the scattering process, the electronic system is in the ground state, i.e., $|i\rangle = |0\rangle$ and $E_i = E_0 = 0$. Equation (2.43) contains two parts, describing two different scattering processes occurring up to second order treatment. The first term is known as non-resonant X-ray scattering (NRIXS), where the momentum transfer $\mathbf{Q} = \mathbf{K}_2 - \mathbf{K}_1$ occurs explicitly [3]. The second term is the resonant inelastic X-ray scattering (RIXS). When the excitation energy ω_1 is far from any excitation energy E_n of the electronic system, the NRIXS term dominates, and the RIXS term vanishes due to the pole structure of the formula. In contrast, for excitation energies ω_1 in resonance with E_n , the RIXS term dominates.

In the case of resonance between ω_1 and E_n , it is convenient to neglect the non-resonant part and rewrite (2.43) using the definition of the transition operator $\hat{T}(\mathbf{e}, \mathbf{K}) = \sum_j \mathbf{e} \cdot \mathbf{p}_j \exp(i\mathbf{K} \mathbf{r}_j)$ as

$$\frac{d^2\sigma}{d\Omega_2 d\omega_2} = \alpha^4 \left(\frac{\omega_2}{\omega_1} \right) \sum_f \left| \sum_n \frac{\langle f | \hat{T}^\dagger(\mathbf{e}_2, \mathbf{K}_2) | n \rangle \langle n | \hat{T}(\mathbf{e}_1, \mathbf{K}_1) | 0 \rangle}{\omega_1 - E_n} \right|^2 \delta(E_f + \omega_2 - \omega_1). \quad (2.44)$$

The physical meaning of this formula on the microscopic scale is the following: An incident X-ray photon with energy ω_1 is absorbed by the sample, initially in its ground state $|0\rangle$. This absorption excites a core electron into the conduction band, leaving a core hole behind and creating an intermediate state $|n\rangle$. Afterwards, the core hole can thus be filled by a valence electron with the emission of a photon ω_2 , leaving a hole in a valence state. The final excited state $|f\rangle$ consists of a hole in this valence state and an excited electron in a conduction state. Consequently, the RIXS final state corresponds to that of a regular optical excitation, as reflected by the small energy loss. Although both the absorbed and emitted photons lie in the X-ray regime, their energy difference $\omega = \omega_1 - \omega_2$ typically amounts to only a few eV. Generally speaking the RIXS process can be classified as a "photon-in-photon-out" scattering process, involving a coherent X-ray absorption followed by an X-ray emission [6]. The energy loss is transferred into the system, resulting in an excited state. A schematic representation of the RIXS process is provided in Figure 1. The following considerations follow closely the work of Christian Vorwerk [3].

Still, this description remains somewhat superficial and lacks a deeper theoretical foundation. A complete interpretation requires considering the interaction between the excited electron and the hole. Furthermore, different types of transitions can lead to the same final excitation, and the coherence of all involved processes must be taken into account. This complexity makes the theoretical description of RIXS challenging. At the same time, its high sensitivity and energy resolution establish it as a powerful technique for studying a wide range of excitations and transitions.

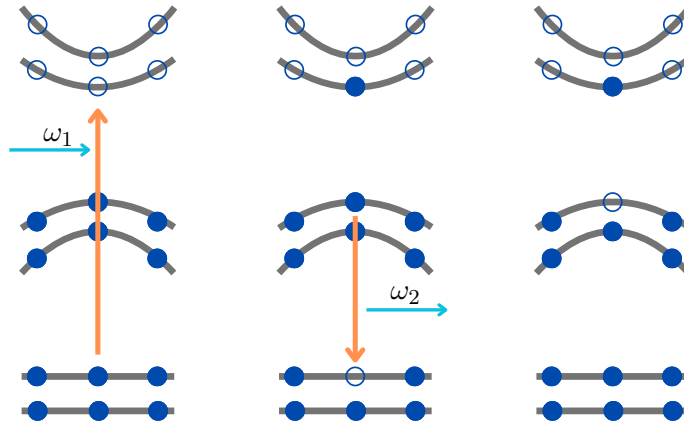


Figure 1: Schema of the direct RIXS process. The absorption of an incoming X-ray photon with energy ω_1 leads to an excited state with a core hole. De-excitation with emission of an X-ray photon with energy ω_2 yields an excited final state with a valence hole. Filled and open circles represent occupied and unoccupied states, respectively. Orange lines represent transitions and light blue lines X-ray absorption and transmission.

2.5.1 Direct and indirect RIXS

There are two different scattering mechanisms that need to be considered: direct and indirect RIXS. So far, only the direct scattering mechanism has been mentioned, which neglects any electron-hole interaction effects. Direct RIXS can already be considered in the independent particle approximation, and both processes, the initial core-to-valence transitions and the final-conduction-to-core transition, must be allowed according to the dipole transition rules, and they occur independently. In contrast, indirect RIXS describes a slightly different process, in which the Coulomb interaction plays a central role. Nonetheless, the strength and significance of this coupling vary with the electronic structure and screening properties of the material. Even if the initial X-ray absorption is weak, the presence of a core hole can lead to additional excitations in form of a secondary electron-hole pair in the intermediate state due to electron-electron interactions, depending on the material and its screening properties. The subsequent de-excitation then occurs from the initially excited electronic state into the core hole, thereby also creating a valence electron-hole pair in the final state [6]. A schematic representation of indirect RIXS is provided in Figure 2. Indirect scattering is primarily observed in systems where the transition from the core state to low-lying conduction states is dipole-forbidden. In this case, quadrupole transitions may also play a role, which are not covered by the generalized Kramers-Heisenberg formula. This effect has been observed, for example, in certain transition metal oxides, such as at the Ni K-edge in NiO and NiCl₂ [53].

2.5.2 RIXS in the independent-particle approximation

As a starting point, it is instructive to discuss the RIXS process within the independent-particle approximation (IPA) before considering the full interacting system described by the BSE. In doing so, again, we closely follow the approach presented by Christian Vorwerk [3].

In the IPA, the many-body ground state wavefunction is given by a single Slater determinant. Both the intermediate state $|n\rangle$ and the final excited state $|f\rangle$ are singlet excitations of the ground state, without any additional relaxations. By definition, the intermediate

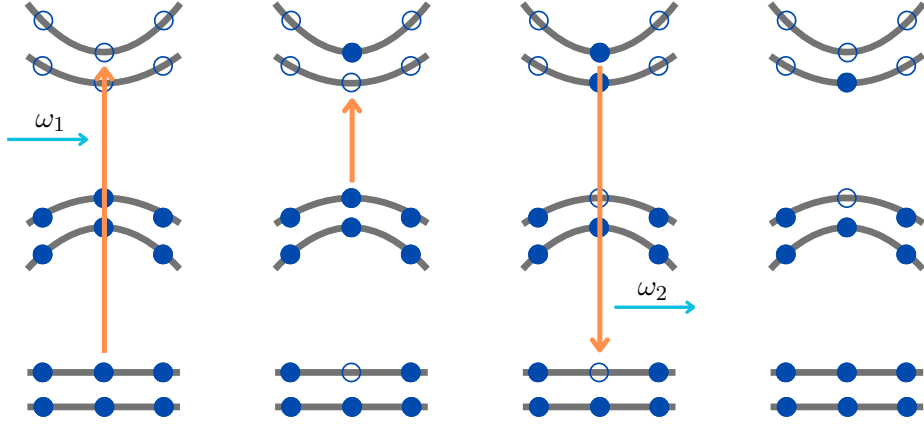


Figure 2: Schema of the indirect RIXS process. The absorption of an incoming X-ray photon with energy ω_1 leads to an excitation into a high-energy conduction state. Excitations from valence to conduction states can be induced by the core-hole potential. Through the emission of an X-ray photon with energy ω_2 , the core-hole is filled, yielding a final excited state containing a valence hole. Filled and open circles represent occupied and unoccupied states, respectively. Orange lines represent transitions and light blue lines X-ray absorption and transmission.

state contains a core hole $\mu\mathbf{k}$ and an electron in a conduction state $c(\mathbf{k} + \mathbf{q}_1)$, while the final state contains an excited electron in a conduction state $c(\mathbf{k}' + \mathbf{q}_2)$ and a valence hole $v\mathbf{k}'$. A momentum transfer $\mathbf{q}_{1/2}$, as a projection of the photon momentum on the first Brillouin zone according to $\mathbf{K}_{1/2} = \mathbf{G}_{1/2} + \mathbf{q}_{1/2}$ with $\mathbf{G}_{1/2}$ being a reciprocal lattice vector, is in principle possible. Employing the dipole approximation, where we make use of the fact that for optical photons the momenta \mathbf{K}_1 and \mathbf{K}_2 of the incoming and scattered photon are small compared to the momenta of the electrons involved in the process. This allows us to rewrite the transition operator as

$$\hat{T}(\mathbf{e}) = \sum_j \mathbf{e} \cdot \mathbf{p}_j \exp(i\mathbf{K}\mathbf{r}_j) \approx \mathbf{e} \sum_j \mathbf{p}_j, \quad (2.45)$$

and to neglect the momentum transfers \mathbf{q}_1 and \mathbf{q}_2 . In second quantization, the intermediate state can be expressed as $|n\rangle = |c\mu\mathbf{k}\rangle = \hat{c}_{c\mathbf{k}}^\dagger \hat{c}_{\mu\mathbf{k}} |0\rangle$ and the final state as $|f\rangle = |c'v\mathbf{k}'\rangle = \hat{c}_{c'\mathbf{k}'}^\dagger \hat{c}_{v\mathbf{k}'} |0\rangle$ with energies $E_n = \epsilon_{c\mathbf{k}} - \epsilon_{\mu\mathbf{k}}$ and $E_f = \epsilon_{c'\mathbf{k}'} - \epsilon_{v\mathbf{k}'}$, respectively. Inserting this into the RIXS DDCS (2.44) yields

$$\left. \frac{d^2\sigma}{d\Omega_2 d\omega_2} \right|_{IP} = \alpha^4 \left(\frac{\omega_2}{\omega_1} \right) \sum_{c'v\mathbf{k}'} \left| \sum_{c\mu\mathbf{k}} \frac{\langle c'v\mathbf{k}' | \hat{T}^\dagger(\mathbf{e}_2) | c\mu\mathbf{k} \rangle \langle c\mu\mathbf{k} | \hat{T}(\mathbf{e}_1) | 0 \rangle}{\omega_1 - (\epsilon_{c\mathbf{k}} - \epsilon_{\mu\mathbf{k}}) + i\eta} \right|^2 \delta(\omega - (\epsilon_{c'\mathbf{k}'} - \epsilon_{v\mathbf{k}'})), \quad (2.46)$$

where the first sum over $c'v\mathbf{k}'$ corresponds to the sum over the final states seen before and the second sum over $c\mu\mathbf{k}$ to the sum over the intermediate states. Since we have already made use of second quantization, it is convenient to express the transition operator in the same formalism as

$$\hat{T}(\mathbf{e}) \approx \mathbf{e} \sum_j \mathbf{p}_j = \sum_{mn} \sum_{\mathbf{k}} [\mathbf{e}_1 \cdot \mathbf{P}_{m\mathbf{k}}] \hat{c}_{m\mathbf{k}}^\dagger \hat{c}_{n\mathbf{k}}, \quad (2.47)$$

where $\mathbf{P}_{m\mathbf{k}}$ denotes the momentum matrix elements analogous to (2.39).

Using this formula finally leads to the RIXS cross section as

$$\left. \frac{d^2\sigma}{d\Omega_2 d\omega_2} \right|_{IP} = \alpha^4 \left(\frac{\omega_2}{\omega_1} \right) \sum_{c\nu\mu\mathbf{k}} \left| \frac{[\mathbf{e}_2^* \cdot \mathbf{P}_{\nu\mathbf{k}}][\mathbf{P}_{c\mu\mathbf{k}} \cdot \mathbf{e}_1]}{\omega_1 - (\epsilon_{c\mathbf{k}} - \epsilon_{\mu\mathbf{k}}) + i\eta} \right|^2 \delta(\omega - (\epsilon_{c\mathbf{k}} - \epsilon_{\nu\mathbf{k}})). \quad (2.48)$$

The detailed derivation can be found in Appendix A.4.

Furthermore, we can express the energy conversation with the δ -function

$$\delta(\omega - E) = \lim_{\eta \rightarrow 0^+} -\frac{1}{\pi} \text{Im} \frac{1}{\omega - E + i\eta}, \quad (2.49)$$

assuming that the intermediate states and the final states share the same lifetime broadening η . Inserting this into Eq. (2.48) finally yield the RIXS DDCCS within the independent particle approximation as

$$\left. \frac{d^2\sigma}{d\Omega_2 d\omega_2} \right|_{IP} = -\alpha^4 \left(\frac{\omega_2}{\omega_1} \right) \text{Im} \sum_{c\nu\mathbf{k}} \frac{\left| \sum_{\mu} \frac{[\mathbf{e}_2^* \cdot \mathbf{P}_{\nu\mathbf{k}}][\mathbf{P}_{c\mu\mathbf{k}} \cdot \mathbf{e}_1]}{\omega_1 - (\epsilon_{c\mathbf{k}} - \epsilon_{\mu\mathbf{k}}) + i\eta} \right|^2}{\omega - (\epsilon_{c\mathbf{k}} - \epsilon_{\nu\mathbf{k}}) + i\eta}. \quad (2.50)$$

2.5.3 RIXS in many-body perturbation theory

Up to now, a compact version of the RIXS cross section was derived within the IPA. However, the neglect of electron-hole interactions may significantly affect the final results. An alternative approach is provided by the application of many-body perturbation theory in the context of RIXS. To this end, all relevant quantities must be expressed in terms of the results of BSE calculations. The derivation follows closely Ref. [3] and can be found in Appendix A.5. In this derivation, it is assumed that both intermediate and final state are singlet excitations, limiting our description to direct RIXS aligning with the Tamm-Dancoff approximation employed in the BSE. The generalized RIXS cross section is finally obtained as

$$\begin{aligned} \left. \frac{d^2\sigma}{d\Omega_2 d\omega_2} \right|_{IP} = & \alpha^4 \left(\frac{\omega_2}{\omega_1} \right) \text{Im} \sum_{cc'c''c'''} \sum_{\mu\mu'\mu''\mu'''} \sum_{\nu\nu'} \sum_{\mathbf{k}\mathbf{k}'\mathbf{k}''\mathbf{k}'''} \left[\left[\mathbf{e}_2^* \cdot \mathbf{P}_{\nu\mathbf{k}} \right] \chi_{c\mu\mathbf{k},c'\mu'\mathbf{k}'}(\omega_1) \left[\mathbf{e}_1 \cdot \mathbf{P}_{c'\mu'\mathbf{k}'} \right] \right]^* \\ & \times \chi_{c\nu\mathbf{k},c''\nu'\mathbf{k}'}(\omega) \left[\left[\mathbf{e}_2^* \cdot \mathbf{P}_{\mu''\nu'\mathbf{k}''} \right] \chi_{c''\mu''\mathbf{k}'',c'''\mu'''\mathbf{k}'''}(\omega_1) \left[\mathbf{e}_1 \cdot \mathbf{P}_{c'''\mu'''\mathbf{k}'''} \right] \right]. \end{aligned} \quad (2.51)$$

Here, the RIXS DDCCS is fully described in terms of the polarizability χ , which is evaluated thrice at two different energies: twice at the initial excitation energy ω_1 , and once at the energy loss $\omega = \omega_1 - \omega_2$. The momentum matrix elements between core and conduction state $\mathbf{P}_{c\mu\mathbf{k}}$ and between valence and core state $\mathbf{P}_{\nu\mathbf{k}}$ correspond to the excitation and de-excitation process, respectively. While this equation may still seem quite complicated, it should be noted that all remaining summations are quite straight forward. The many-body character of the system is captured only implicitly through the polarizability, so that, for a given polarizability, an explicit evaluation becomes feasible.

To evaluate this expression within the framework of MBPT, it is convenient to express the cross section in terms of quantities obtained from a BSE calculation. Following Eq. (2.37), the polarizability is given by

$$\chi_{ij\mathbf{k},i'j'\mathbf{k}'}(\omega) = \sum_{\lambda} \frac{\left[A_{ij\mathbf{k}}^{\lambda} \right]^* A_{i'j'\mathbf{k}'}^{\lambda}}{\omega - E^{\lambda} + i\eta}, \quad (2.52)$$

where $A_{ou\mathbf{k}}^\lambda$ and E^λ are the BSE eigenstates and eigenvalues, respectively. Considering the second bracket in Eq.(2.51) and insert the explicit form of the polarizability, one gets

$$\begin{aligned}
 & \sum_{c'''\mu'''\mathbf{k}'''} \sum_{\mu''} [\mathbf{e}_2^* \cdot \mathbf{P}_{\mu''v'\mathbf{k}''}] \chi_{c''\mu''\mathbf{k}'',c'''\mu'''\mathbf{k}'''}(\omega_1) [\mathbf{e}_1 \cdot \mathbf{P}_{c'''\mu'''\mathbf{k}'''}] \\
 &= \sum_{c'''\mu'''\mathbf{k}'''} \sum_{\mu''} \sum_{\lambda_c} [\mathbf{e}_2^* \cdot \mathbf{P}_{\mu''v'\mathbf{k}''}] \frac{[A_{c''\mu''\mathbf{k}''}^{\lambda_c}]^* A_{c'''\mu'''\mathbf{k}'''}^{\lambda_c}}{\omega_1 - E^{\lambda_c} + i\eta} [\mathbf{e}_1 \cdot \mathbf{P}_{c'''\mu'''\mathbf{k}'''}] \\
 &= \sum_{\mu''} \sum_{\lambda_c} [\mathbf{e}_2^* \cdot \mathbf{P}_{\mu''v'\mathbf{k}''}] \frac{[A_{c''\mu''\mathbf{k}''}^{\lambda_c}]^* t_{\lambda_c}^{(1)}}{\omega_1 - E^{\lambda_c} + i\eta}.
 \end{aligned} \tag{2.53}$$

In the last step, we have defined the core excitation oscillator strength $t_{\lambda_c}^{(1)}$ as

$$t_{\lambda_c}^{(1)} = \sum_{c'''\mu'''\mathbf{k}'''} A_{c'''\mu'''\mathbf{k}'''}^{\lambda_c} [\mathbf{e}_1 \cdot \mathbf{P}_{c'''\mu'''\mathbf{k}'''}], \tag{2.54}$$

which describes the core absorption step in the RIXS process. The RIXS DDCS then becomes

$$\begin{aligned}
 \frac{d^2\sigma}{d\Omega_2 d\omega_2} &= \alpha^4 \left(\frac{\omega_2}{\omega_1} \right) \text{Im} \sum_{\lambda_c, \lambda_c', \lambda_0} \sum_{cc'} \sum_{vv'} \sum_{\mathbf{k}\mathbf{k}''} \left[\sum_{\mu} \frac{t_{\lambda_c'}^{(1)} [A_{c\mu\mathbf{k}}^{\lambda_c'}]^* [\mathbf{e}_2^* \cdot \mathbf{P}_{\mu v\mathbf{k}}]}{\omega_1 - E^{\lambda_c'} + i\eta} \right]^* \\
 &\times \frac{[A_{cv\mathbf{k}}^{\lambda_0}]^* A_{c''v'\mathbf{k}''}^{\lambda_0}}{\omega - E^{\lambda_0} + i\eta} \left[\sum_{\mu''} \frac{[\mathbf{e}_2^* \cdot \mathbf{P}_{\mu''v'\mathbf{k}''}] A_{c''\mu''\mathbf{k}''}^{\lambda_c} t_{\lambda_c}^{(1)}}{\omega_1 - E^{\lambda_c} + i\eta} \right].
 \end{aligned} \tag{2.55}$$

Here, λ_0 denotes valence-conduction excitations, whereas λ_c refers to core-conduction excitations. It is convenient to define the excitation pathway $t_{\lambda_0, \lambda_c}^{(2)}$ as

$$t_{\lambda_0, \lambda_c}^{(2)} = \sum_{c\mathbf{v}\mathbf{k}} \sum_{\mu} A_{c\mathbf{v}\mathbf{k}}^{\lambda_0} [\mathbf{e}_2^* \cdot \mathbf{P}_{\mu v\mathbf{k}}] [A_{c\mu\mathbf{k}}^{\lambda_c}]^*, \tag{2.56}$$

which allows us to simplify the DDCS to

$$\frac{d^2\sigma}{d\Omega_2 d\omega_2} = \alpha^4 \left(\frac{\omega_2}{\omega_1} \right) \text{Im} \sum_{\lambda_0} \frac{\left| \sum_{\lambda_c} \frac{t_{\lambda_0, \lambda_c}^{(2)} t_{\lambda_c}^{(1)}}{\omega_1 - E^{\lambda_c} + i\eta} \right|^2}{\omega - E^{\lambda_0} + i\eta}. \tag{2.57}$$

Finally, we define the RIXS oscillator strength $t_{\lambda_0}^{(3)}(\omega_1)$ as

$$t_{\lambda_0}^{(3)}(\omega_1) = \sum_{\lambda_c} \frac{t_{\lambda_0, \lambda_c}^{(2)} t_{\lambda_c}^{(1)}}{\omega_1 - E^{\lambda_c} + i\eta}, \tag{2.58}$$

which yields the RIXS double-differential cross section

$$\frac{d^2\sigma}{d\Omega_2 d\omega_2} = \alpha^4 \left(\frac{\omega_2}{\omega_1} \right) \text{Im} \sum_{\lambda_0} \frac{|t_{\lambda_0}^{(3)}(\omega_1)|^2}{\omega - E^{\lambda_0} + i\eta} = \alpha^4 \left(\frac{\omega_2}{\omega_1} \right) \text{Im} \sum_{\lambda_0} \frac{|t_{\lambda_0}^{(3)}(\omega_1)|^2}{(\omega_1 - \omega_2) - E^{\lambda_0} + i\eta}. \tag{2.59}$$

This compact formulation in terms of the three oscillator strengths $t_{\lambda_c}^{(1)}$, $t_{\lambda_0, \lambda_c}^{(2)}$, and $t_{\lambda_0}^{(3)}(\omega_1)$ offers several advantages. First, the cross section depends explicitly on the energy loss

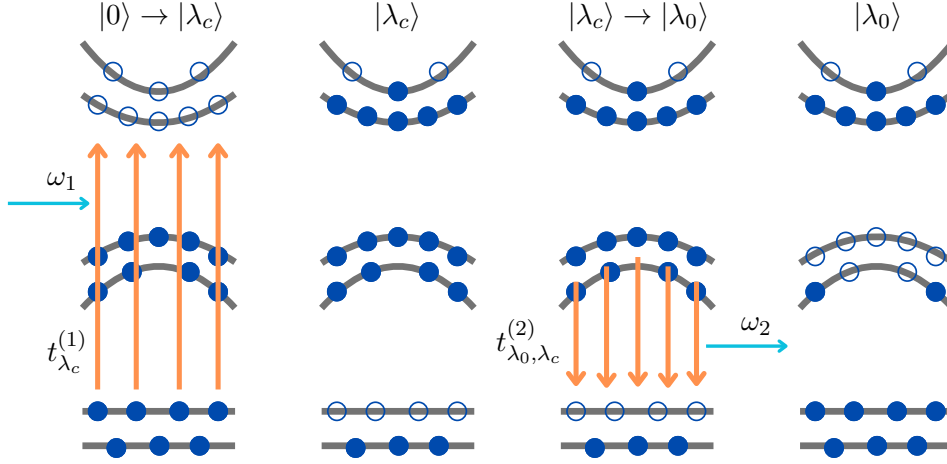


Figure 3: Schema of the RIXS process within MBPT. Starting from the ground state $|0\rangle$, the absorption of an incoming X-ray photon with energy ω_1 yields an intermediate many-body state $|\lambda_c\rangle$. Subsequent de-excitation through emission of an X-ray photon ω_2 yields an excited final state $|\lambda_0\rangle$ containing valence electron-hole pairs. Filled and open circles represent occupied and unoccupied states, respectively. Orange lines represent transitions and light blue lines X-ray absorption and transmission.

$\omega = \omega_1 - \omega_2$, while the RIXS oscillator strength solely depends on the excitation energy ω_1 . Moreover, the two oscillator strengths $t_{\lambda_c}^{(1)}$ and $t_{\lambda_0, \lambda_c}^{(2)}$ depend neither on the excitation energy nor the energy loss and therefore need to be calculated only once from the solution of the BSE for optical and core excitations. This is also reflected in the indices of the eigenvalues A^λ in Eq. (2.55). The denominator of Eq. (2.59) enforces energy conservation throughout the process and defines the poles of the cross section at energy losses corresponding to the optical excitation energies E^{λ_0} . While these energies are, in principle, independent of the incident photon energy, the spectral intensity varies with it through $t_{\lambda_0}^{(3)}(\omega_1)$.

Furthermore, this expression allows for an intuitive interpretation of the RIXS process itself, illustrated in Figure 3. The initial X-ray absorption rate is given by $t_{\lambda_c}^{(1)}$ in combination with the energy conservation. The absorption from the ground state $|0\rangle$ leads to an intermediate state $|\lambda_c\rangle$, indicated by the excitation index λ_c inside the oscillator strength $t_{\lambda_c}^{(1)}$. The final RIXS emission results from de-excitation process $|\lambda_c\rangle \rightarrow |\lambda_0\rangle$, described by the excitation pathway $t_{\lambda_0, \lambda_c}^{(2)}$, combined with the initial absorption. The resulting structure of $t_{\lambda_0}^{(3)}(\omega_1)$ is highly non-trivial and can lead to constructive and destructive interference effects. Moreover, this approach captures incoherent scattering effects beyond the IPA, enabling absorption and emission to occur at different \mathbf{k} -points.

In deriving these results, only minimal approximations were used. Beyond the limitation onto direct RIXS within the TDA, the formulation is in principal exact, under the assumption of accurate BSE results in form of eigenvectors and -values. Consequently, the reliability of RIXS calculations is directly tied to the accuracy of the underlying DFT and BSE calculations.

3 Methods

The theoretical foundations relevant to this work have been introduced in the previous chapter. In the following, the practical implementation and computational methods used in this thesis are described. Ground-state and excited-state properties were calculated using the all-electron full-potential code **exciting**, which implements density-functional theory (DFT) and many-body perturbation theory including the Bethe–Salpeter equation (BSE). For the calculation of resonant inelastic X-ray scattering (RIXS) spectra, the BRIXS framework was employed.

3.1 Numerical solution of DFT in exciting

exciting [54] is an all-electron, full-potential electronic-structure package. It implements the (L)APW+lo methods on the Kohn-Sham level, achieving exceptional precision [55]. We closely follow Ref. [56], where the implementation of the basis sets within **exciting** is explained in detail.

To apply a dual-basis method, the unit-cell is divided in non-overlapping regions, named muffin-tin spheres (MT), centered at the atomic positions and the region between these spheres, called the interstitial region (I).

While wavefunctions far away from the nuclei vary slowly and can be expanded in plane waves easily, they behave differently in vicinity of the cores and would require a high number of plane waves to describe the localized behavior and rapid oscillations. Therefore, a separation into muffin-tin and interstitial region is convenient. While in the I-region plane waves are used, inside the MT-region the wave function is described by atomic-like orbitals. This dual-basis approach combines the strengths of both basis sets, enabling accurate and computationally efficient representations of the wavefunction. The basis functions are defined as

$$\phi_{\mathbf{k}+\mathbf{G}}(\mathbf{r}) = \begin{cases} \frac{1}{\sqrt{\Omega}} e^{-i(\mathbf{G}+\mathbf{k})\mathbf{r}} & \mathbf{r} \in I \\ \sum_{lm,p} A_{lm,p}^{\mathbf{k}+\mathbf{G}} u_{l,p}^{\alpha}(r) Y_{lm}(\hat{r}) & \mathbf{r} \in MT, \end{cases} \quad (3.1)$$

with Ω the unit-cell volume, and the coefficients $A_{lm,p}^{\mathbf{k}+\mathbf{G}}$ ensure the continuity of the basis functions at the MT boundaries. The atomic-like function consists of linear combinations of radial functions multiplied with spherical harmonics $Y_{lm}(\hat{r})$. The radial functions are solutions of the radial Schrödinger equation using the spherically averaged Kohn-Sham potential in the respective atomic sphere. The index p indicates the order of the derivative w.r.t. the energy, i.e., $u_{l,p}^{\alpha} = \frac{\partial^p u_l^{\alpha}}{\partial \epsilon^p}$. While $p = 0$ yields the APW basis set, the summation up to $p = 1$ yields the LAPW basis set. Higher orders could also be included. By including the energy derivative of the radial functions, the nonlinear dependence on the energy ϵ is resolved, since one can appropriately choose fixed trial energies in the solution of the radial Schrödinger equation, and the method becomes linearized. To increase the variational degree of freedom, local orbitals (LOs) are introduced. Analogous to the LAPWs, they have an atomic-orbital-like form inside the MT sphere, but vanish in the interstitial region. They are described by

$$\phi_v(\mathbf{r}) = \begin{cases} 0 & \mathbf{r} \in I \\ \delta_{\alpha\alpha_v} \delta_{ll_v} \delta_{mm_v} \sum_p B_{v,p} u_{l,p}^{\alpha}(r) Y_{lm}(\hat{r}) & \mathbf{r} \in MT, \end{cases} \quad (3.2)$$

with the expansion coefficients $B_{v,p}$ ensuring that the basis is continuous up to the first derivative at the sphere boundaries [57]. Adding these LOs for specific MT spheres and (lm)-channels yields a significant improvement of the basis. In particular, semicore states,

constructed with different linearization energies, can be described more accurately. Finally, in the LAPW+lo basis the wavefunction $\psi_{i\mathbf{k}}^{\text{KS}}$ of the Kohn-Sham Hamiltonian are given by

$$\psi_{i\mathbf{k}}^{\text{KS}} = \sum_{\mathbf{G}} C_{i(\mathbf{k}+\mathbf{G})} \phi_{\mathbf{k}+\mathbf{G}}(\mathbf{r}) + \sum_v C_{iv\mathbf{k}} \phi_v(\mathbf{r}) \quad (3.3)$$

with

$$u_l^{i\mathbf{k}} = \sum_p \sum_{\mathbf{G}} C_{i(\mathbf{k}+\mathbf{G})} A_{lm,p}^{\mathbf{k}+\mathbf{G}} u_{l,p}^\alpha(r) + \sum_v C_{iv\mathbf{k}} B_{v,p} u_{l,p}^\alpha(r) \quad (3.4)$$

using the expansion coefficients $C_{i(\mathbf{k}+\mathbf{G})}$ and $C_{iv\mathbf{k}}$ obtained from the diagonalization of the Kohn-Sham Hamiltonian, i.e., by solving a generalized eigenvalue problem $HC = \epsilon SC$, where H and S are the Hamiltonian and the overlap matrices constructed in the LAPW+lo basis.

While this expansion works well for valence and conduction states, a different treatment is necessary for the consideration of the highly localized core states. These electrons, due to their proximity to the core, need to be treated fully relativistically to consider spin-orbit coupling. Therefore the radial Dirac equation for a spherical harmonic potential needs to be solved. The spinor solution can be written as

$$\psi_{\kappa,M}^{\text{KS}} = \begin{pmatrix} u_\kappa(r) \Omega_{\kappa,M}(\hat{r}) \\ -iv_\kappa(r) \Omega_{-\kappa,M}(\hat{r}) \end{pmatrix}, \quad (3.5)$$

where the unique core index κ was introduced for a core state $^{2S+1}L_J$ as

$$\kappa = \begin{cases} -L - 1 & \text{for } J = L + \frac{1}{2} \\ L & \text{for } J = L - \frac{1}{2}. \end{cases} \quad (3.6)$$

The quantum numbers (L, J, M) are not independent because $J = L \pm \frac{1}{2}$. Therefore the spin spherical harmonics can be expressed as

$$\Omega_{L \pm \frac{1}{2}, M}(\hat{\mathbf{r}}) = \begin{pmatrix} \pm \sqrt{\frac{L \pm M + \frac{1}{2}}{2L+1}} Y_{L, M \mp \frac{1}{2}}(\hat{\mathbf{r}}) \\ \sqrt{\frac{L \mp M + \frac{1}{2}}{2L+1}} Y_{L, M \pm \frac{1}{2}}(\hat{\mathbf{r}}) \end{pmatrix}. \quad (3.7)$$

Consequently, the core wavefunctions are four-dimensional Dirac spinors with the large components, containing u_κ , and the small components, containing v_κ . The radial functions $u_\kappa(r)$ for the large components and $v_\kappa(r)$ for the small components are obtained by solving the coupled radial Dirac equations

$$\frac{\partial u_\kappa}{\partial r} = \frac{1}{c} (v_{\text{eff}} - \epsilon_\kappa) v_\kappa + \frac{\kappa - 1}{r} u_\kappa \quad (3.8)$$

$$\frac{\partial v_\kappa}{\partial r} = -\frac{\kappa + 1}{r} v_\kappa + 2c \left[1 + \frac{1}{2c^2} (\epsilon_\kappa - v_{\text{eff}}) \right]. \quad (3.9)$$

Here v_{eff} denotes the spherical averaged Kohn-Sham potential. For the calculation of matrix elements between core and conduction states, we neglect the small component. The KS core wavefunction at an atomic site α is then obtained as

$$\psi_{\kappa,M}^\alpha = \begin{cases} u_{\alpha,\kappa}(r_\alpha) \Omega_{\kappa,M}(\hat{r}_\alpha) & \text{for } r_\alpha \leq R_{MT} \\ 0 & \text{else} \end{cases} \quad (3.10)$$

Additional information regarding the implementation within **exciting** can be found in Refs. [54, 58]. For a more detailed discussion of time-dependent density-functional theory, we refer to Refs. [59–62].

3.2 Numerical solution of the BSE eigenvalue problem in exciting

We next describe the implementation of the BSE formalism within **exciting**. Further reading is provided in [56, 57, 60]. As discussed in Section 2.4.3, the construction of the BSE Hamiltonian requires the quasi-particle energies, which we can obtain from either DFT or *GW*. First, we want to consider how the different matrix elements are constructed within **exciting**.

The momentum matrix elements $P_{nm\mathbf{k}}^j$ between conduction and valence states, with j indicating the polarization of the incoming light, are expanded in the LAPW+lo basis as

$$\begin{aligned} P_{nm\mathbf{k}}^j &= \langle n\mathbf{k} | -i\nabla_j | m\mathbf{k} \rangle \\ &= \sum_{\mathbf{G}, \mathbf{G}'} C_{n(\mathbf{k}+\mathbf{G})}^* C_{m(\mathbf{k}+\mathbf{G})} P_{\mathbf{G}\mathbf{G}'\mathbf{k}}^j + \sum_{\mathbf{G}, v} C_{n(\mathbf{k}+\mathbf{G})}^* C_{mv\mathbf{k}} P_{\mathbf{G}v\mathbf{k}}^j \\ &\quad + \sum_{\mathbf{G}', v'} C_{mv'\mathbf{k}}^* C_{n(\mathbf{k}+\mathbf{G})} P_{v'\mathbf{G}'\mathbf{k}}^j + \sum_{v, v'} C_{mv'\mathbf{k}}^* C_{nv\mathbf{k}} P_{v'v\mathbf{k}}^j, \end{aligned} \quad (3.11)$$

with the coefficients $C_{i\mathbf{k}}$ and $C_{iv\mathbf{k}}$ of the KS eigenstates $\psi_{i\mathbf{k}}^{\text{KS}}$. $P_{\mathbf{G}\mathbf{G}'\mathbf{k}}^j$, $P_{\mathbf{G}v\mathbf{k}}^j$, $P_{v'\mathbf{G}'\mathbf{k}}^j$, and $P_{v'v\mathbf{k}}^j$ are the LAPW-LAPW, LAPW-LO, LO-LAPW, and LO-LO momentum matrix elements, respectively, defined as

$$\begin{aligned} P_{\mathbf{G}\mathbf{G}'\mathbf{k}}^j &= \langle \phi_{\mathbf{k}+\mathbf{G}} | -i\nabla_j | \phi_{\mathbf{k}+\mathbf{G}'} \rangle, & P_{\mathbf{G}v\mathbf{k}}^j &= \langle \phi_{\mathbf{k}+\mathbf{G}} | -i\nabla_j | \phi_v \rangle, \\ P_{v'\mathbf{G}'\mathbf{k}}^j &= \langle \phi_{v'} | -i\nabla_j | \phi_{\mathbf{k}+\mathbf{G}'} \rangle, & P_{v'v\mathbf{k}}^j &= \langle \phi_{v'} | -i\nabla_j | \phi_v \rangle. \end{aligned} \quad (3.12)$$

Each momentum matrix element P_{nm}^j can be decomposed into MT-sphere and I-region contributions. Since local orbitals vanish in the interstitial region, only $P_{\mathbf{G}\mathbf{G}'}^j$ has non-vanishing contributions. The interstitial part of the matrix elements can be calculated analytically. For the MT sphere, the action of the momentum-operator is expanded in terms of spherical harmonics. This allows for an analytic expression of the spherical integrals, while the radial integration is performed numerically.

The plane-wave matrix elements $M_{m\mathbf{n}\mathbf{k}}(\mathbf{G}, \mathbf{q})$ are calculated as

$$\begin{aligned} M_{m\mathbf{n}\mathbf{k}}(\mathbf{G}, \mathbf{q}) &= \langle m\mathbf{k} | e^{-i(\mathbf{G}+\mathbf{q})\mathbf{r}} | n(\mathbf{k}+\mathbf{q}) \rangle \\ &= \sum_{\mathbf{G}', \mathbf{G}''} C_{m(\mathbf{k}+\mathbf{G}')}^* C_{n(\mathbf{k}+\mathbf{q}+\mathbf{G}'')} M_{\mathbf{G}'\mathbf{G}''\mathbf{k}}(\mathbf{G}, \mathbf{q}) + \sum_{\mathbf{G}', v'} C_{m(\mathbf{k}+\mathbf{G}')}^* C_{nv'\mathbf{k}} M_{\mathbf{G}'v'\mathbf{k}}(\mathbf{G}, \mathbf{q}) \\ &\quad + \sum_{\mathbf{G}', v} C_{mv'\mathbf{k}}^* C_{n(\mathbf{k}+\mathbf{q}+\mathbf{G}')} M_{v\mathbf{G}'\mathbf{k}}(\mathbf{G}, \mathbf{q}) + \sum_{v, v'} C_{mv'\mathbf{k}}^* C_{nv(\mathbf{k}+\mathbf{q})} M_{vv'\mathbf{k}}(\mathbf{G}, \mathbf{q}), \end{aligned} \quad (3.13)$$

where the LAPW-LAPW, LAPW-LO, LO-LAPW, and LO-LO plane-wave matrix elements are given by

$$\begin{aligned} M_{\mathbf{G}\mathbf{G}'\mathbf{k}}(\mathbf{G}, \mathbf{q}) &= \langle \phi_{\mathbf{k}+\mathbf{G}} | e^{-i(\mathbf{G}+\mathbf{q})\mathbf{r}} | \phi_{\mathbf{k}+\mathbf{q}+\mathbf{G}'} \rangle, & M_{\mathbf{G}'v\mathbf{k}}(\mathbf{G}, \mathbf{q}) &= \langle \phi_{\mathbf{k}+\mathbf{G}'} | e^{-i(\mathbf{G}+\mathbf{q})\mathbf{r}} | \phi_v \rangle, \\ M_{v'\mathbf{G}'\mathbf{k}}(\mathbf{G}, \mathbf{q}) &= \langle \phi_{v'} | e^{-i(\mathbf{G}+\mathbf{q})\mathbf{r}} | \phi_{\mathbf{k}+\mathbf{q}+\mathbf{G}'} \rangle, & M_{vv'\mathbf{k}}(\mathbf{G}, \mathbf{q}) &= \langle \phi_v | e^{-i(\mathbf{G}+\mathbf{q})\mathbf{r}} | \phi_{v'} \rangle. \end{aligned} \quad (3.14)$$

Also the plane-wave matrix elements are decomposed in an interstitial and a MT part. The interstitial part is calculated analytically. Again, in the MT region, the spherical integration is performed analytically while the radial integration is performed numerically on the radial grid.

Using these matrix elements, we can now expand the interaction kernels in plane waves, as outlined in Sec. 2.4.3. In the optical limit, corresponding to vertical transitions and vanishing momentum transfer $q \rightarrow 0$, the BSE can be expressed in terms of a combined

transition index α , of (o, u, \mathbf{k}) . We will omit the explicit \mathbf{q} -dependence in the following and express the matrix elements of the exchange interaction H^x as

$$H_{\alpha\alpha'}^x(\mathbf{q}) = \sum_{\mathbf{G}} v_{\mathbf{G}}(\mathbf{q}) M_{uok_-}^*(\mathbf{G}, \mathbf{q}) M_{u'o'k'_-}(\mathbf{G}, \mathbf{q}). \quad (3.15)$$

Here, the Fourier transform of the bare Coulomb potential

$$v(\mathbf{r}, \mathbf{r}') = \sum_{\mathbf{G}} \sum_{\mathbf{p}} \frac{1}{\Omega} \frac{4\pi}{|\mathbf{G} + \mathbf{p}|^2} e^{i(\mathbf{G} + \mathbf{p})(\mathbf{r} - \mathbf{r}')} \equiv \sum_{\mathbf{G}} \sum_{\mathbf{p}} v_{\mathbf{G}}(\mathbf{p}) e^{i(\mathbf{G} + \mathbf{p})(\mathbf{r} - \mathbf{r}')} \quad (3.16)$$

was introduced. We express the statically screened Coulomb potential

$$w(\mathbf{r}, \mathbf{r}') = \int d^3r'' v(\mathbf{r}, \mathbf{r}'') \epsilon^{-1}(\mathbf{r}'', \mathbf{r}', \omega = 0), \quad (3.17)$$

as a plane-wave expansion

$$w(\mathbf{r}, \mathbf{r}') = \sum_{\mathbf{G}\mathbf{G}'} \sum_{\mathbf{p}} e^{i(\mathbf{G} + \mathbf{p})\mathbf{r}} w_{\mathbf{G}\mathbf{G}'}(\mathbf{p}, \omega = 0) e^{-i(\mathbf{G}' + \mathbf{p})\mathbf{r}'} \quad (3.18)$$

with the Fourier components defined as

$$w_{\mathbf{G}\mathbf{G}'}(\mathbf{p}) = v_{\mathbf{G}}(\mathbf{p}) \epsilon_{\mathbf{G}\mathbf{G}'}^{-1}(\mathbf{p}, \omega = 0). \quad (3.19)$$

The dielectric tensor is computed within the random-phase approximation (RPA) as

$$\epsilon_{\mathbf{G}\mathbf{G}'}(\mathbf{q}, \omega) \approx \epsilon_{\mathbf{G}\mathbf{G}'}^{\text{RPA}}(\mathbf{q}, \omega) = \delta_{\mathbf{G}\mathbf{G}'} - \frac{1}{\Omega_0} v_{\mathbf{G}'}(\mathbf{q}) \sum_{ijk} \frac{f(\epsilon_{j\mathbf{k}+\mathbf{q}}) - f(\epsilon_{i\mathbf{k}})}{\epsilon_{j\mathbf{k}+\mathbf{q}} - \epsilon_{i\mathbf{k}} - \omega} [M_{ij}^{\mathbf{G}}(\mathbf{k}, \mathbf{q})]^* M_{ij}^{\mathbf{G}'}(\mathbf{k}, \mathbf{q}). \quad (3.20)$$

Here, $f(\epsilon_{i\mathbf{k}})$ denotes the occupation factor of the corresponding single-particle state with energy $\epsilon_{i\mathbf{k}}$. Thus, the BSE matrix elements of the screened Coulomb interaction are given by

$$H_{\alpha\alpha'}^c(\mathbf{q}) = \sum_{\mathbf{G}, \mathbf{G}'} w_{\mathbf{G}, \mathbf{G}'}(\mathbf{k} - \mathbf{k}') M_{o'o\mathbf{k}'_+}^*(\mathbf{G}, \mathbf{k} - \mathbf{k}') M_{u'u\mathbf{k}'_-}^*(\mathbf{G}, \mathbf{k} - \mathbf{k}'). \quad (3.21)$$

Taking these different contributions together, the full BSE Hamiltonian is assembled, and the eigenvalue problem is solved via matrix diagonalization, as described in Section 2.4.3. Since this diagonalizing step is computationally highly demanding, it represents the bottleneck of solving the BSE in **exciting**. Main numerical parameters are the numbers of valence and conduction states N_v and N_c , respectively, and the size of the Brillouin zone \mathbf{k} -grid N_k . While the construction of the BSE Hamiltonian scales with $\mathcal{O}(N_k^2 N_v^2 N_c^2)$, the diagonalization scales even worse with $\mathcal{O}(N_k^3 N_v^3 N_c^3)$.

3.3 Numerical solution of resonant inelastic X-ray scattering

RIXS spectra can be computed from first principles by making use of the implementation of the Bethe–Salpeter equation. In this section, the practical computation of RIXS within the BRIS framework is described. Starting from BSE results obtained using **exciting**, the code evaluates the relevant matrix elements and oscillator strengths required to determine the RIXS cross section. Particular focus is given to the treatment of polarization vectors and extensions enabling quantitative comparison with experiments.

3.3.1 RIXS pathways from BSE in BRIXS

BRIXS [63] is a code by Christian Vorwerk for calculations of **RIXS** spectra based on BSE calculations. Detailed information are provided in his dissertation [3]. Further applications include studies on RIXS for LiF [4], diamond, and Ga₂O₃ [5]. The code takes the output of two BSE calculations and calculates the oscillator strength $t^{(1)}$ of the core excitation, the excitation pathway $t^{(2)}$, and the RIXS oscillator strength $t^{(3)}(\omega_1)$. As described in Section 2.5, the calculation of the single pathways requires the eigenstates $A_{c\nu\mathbf{k}}^{\lambda_0}$ and eigenenergies E^{λ_0} of the optical excitation and the eigenstates $A_{c\mu\mathbf{k}}^{\lambda_c}$ and eigenenergies E^{λ_c} of the core excitation for a specific absorption edge. Furthermore, the momentum matrix elements $\mathbf{P}_{c\mu\mathbf{k}}$ and $\mathbf{P}_{\nu\mathbf{k}}$ are required.

A BRIXS calculation is separated into two independent tasks. First, "BRIXS-pathway" determines the matrices $t^{(1)}$ and $t^{(2)}$. Second, "BRIXS-oscstr" takes the results from the previous task and calculates the matrix $t^{(3)}(\omega_1)$ for a given list of excitation energies ω_1 . The reason for this separation into two tasks is the following: While the calculation of $t^{(1)}$ and $t^{(2)}$ is universal for given BSE results, only the calculation of $t^{(3)}(\omega_1)$ depends on the excitation energy. The determination of the DDCS in Eq. (2.59) is carried out in the python module `pyBRIXS` [64]. Starting from the RIXS oscillator strength $t^{(3)}(\omega_q)$, the RIXS DDCS can be calculated for arbitrary values for the energy loss $\omega = \omega_1 - \omega_2$, choosing a lifetime broadening η .

The BRIXS code requires four files as an input: The results of the two BSE calculations *optical_output.h5* and *core_output.h5*, the momentum matrix elements *pmat.h5*, and the RIXS input file *input.cfg*. Only a small number of input parameters is required: the excitation energies ω_1 , the number of considered core-conduction N_{λ_c} and valence-conduction excitations N_{λ_0} , the lifetime broadening of the intermediate state η , and the polarization vector \mathbf{e}_1 of the photon. The "BRIXS-pathway" program generates an HDF5-file *data.h5*, which contains the matrix elements of $t^{(1)}$ and $t^{(2)}$ as well as the eigenvalues E^{λ_c} of the core excitation. A further file, *rixs.h5*, containing the elements of $t^{(3)}(\omega_1)$, is generated by the program "BRIXS-oscstr".

Up to now, following the initial implementation of BRIXS by Christian Vorwerk [3], identical polarizations of incoming and outgoing photons were assumed and implemented, i.e., $\mathbf{e}_1 = \mathbf{e}_2$. In the scope of this work, we generalized the application to arbitrary polarization vectors \mathbf{e}_1 and \mathbf{e}_2 , given in form of the input parameters p_{in} and p_{out} . According to the expressions for $t^{(1)}$ in Eq. (2.54) and $t^{(2)}$ in Eq. (2.56), the polarization of the incoming photon \mathbf{e}_1 enters the calculation of the core excitation oscillator strength $t^{(1)}$, while the polarization \mathbf{e}_2 of the outgoing photon enters the calculation of the excitation pathway $t^{(2)}$.

While this seems to be quite straight forward, it still implies a major approximation. The derivation of the RIXS properties in Section 2.5 and thus the original implementation were based on the polarizability χ . However, using **exciting** for the calculation of the polarizability, a fixed cartesian direction needs to be selected. Thus, only cartesian polarization directions and identical in- and out-going polarizations were possible for the RIXS calculations. To avoid this, one can alternatively use the reduced polarizability $\bar{\chi}$, neglecting long range Coulomb interactions. It is computed uniformly for all polarization directions, allowing to extract and mix different polarizations for in- and out-going photons while still using only two BSE calculations. Nonetheless, using $\bar{\chi}$ instead of χ does not follow natively from the formulas of RIXS. And even if the difference between both results is small on the level of BSE, that does not a priori ensure comparable results on the level of RIXS, due to its highly non-linear character.

As a benchmark test, we perform two BRIXS calculations for graphite, a layered material with highly different in- and out-of-plane spectra. For the results using χ , two sets of BSE calculations were performed for polarizations lying in-plane or directed out-of-plane. The results obtained via $\bar{\chi}$ only require a single set of BSE calculations. The results are depicted in Fig. 4 and show only minimal differences. All features appear in both RIXS spectra, and minor differences appear only in the intensities at low losses.

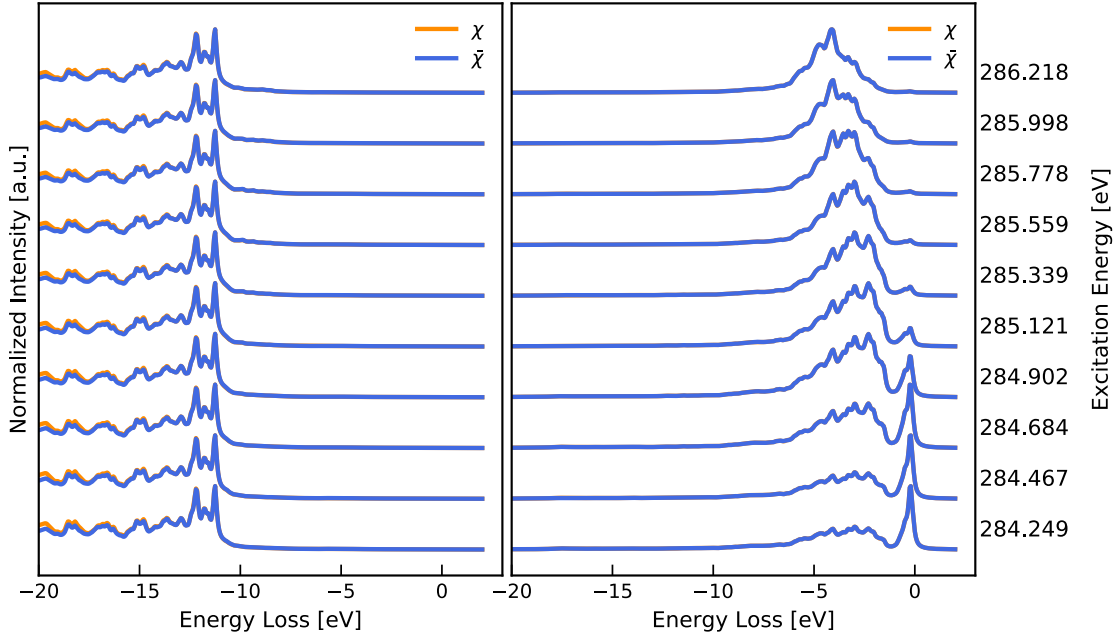


Figure 4: Comparison of BRIXS results for graphite obtained from the full polarizability χ and the reduced polarizability $\bar{\chi}$ for the polarization chosen in the in-plane (left) and the out-of-plane direction (right).

We deduce, that the use of the reduced polarizability $\bar{\chi}$ is a valid approximation, at least for graphite investigated here.

3.3.2 Post processing with pyBRIXS

Once the RIXS oscillator strength is calculated for a given range of initial photon energies, the RIXS double-differential cross-section can be obtained for a given range of energy loss values $\omega = \omega_1 - \omega_2$ and the final-state lifetime broadening η . A convenient way to generate these cross-sections is given by the Python module `pyBRIXS`. Taking the results from a prior BRIXS calculation, the module calculates the cross-sections and also stores other important properties such as the RIXS oscillator strength and the emission energy ω_2 . We additionally developed another extension, based on an implementation provided by Maria Laura Urquiza, to directly store the RIXS DDCS vs. the energy-loss in a separate file. We also included the option to take the average over multiple results. Therefore it is possible to first calculate the RIXS DDCS from multiple BRIXS calculations for a varying range of polarizations $p_{\text{in}}/p_{\text{out}}$ and afterwards calculate the average over these polarizations. This is especially convenient for comparison with experiments, in which either one or both of these quantities may not be fixed.

3.4 Workflow

The whole workflow to calculate equilibrium and non-equilibrium RIXS results, consists of a compilation of various steps, schematically displayed in Fig. 5. In a first step, DFT

ground state calculations are performed and act as a basis for the following BSE calculations for both optical and core level x-ray absorption spectra. For studying systems out of equilibrium, RT-TDDFT is employed as an additional step between DFT and BSE, to calculate the non-equilibrium occupations and build the basis for subsequent constraint BSE calculations.

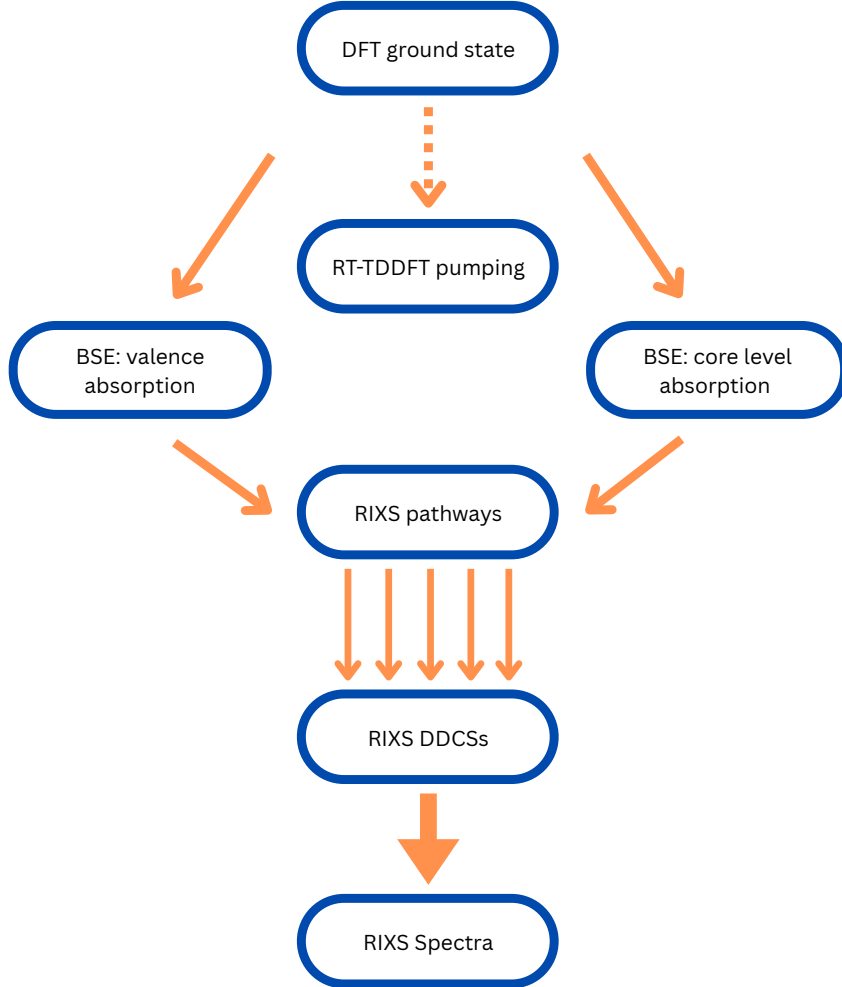


Figure 5: Schematic representation of the workflow: A DFT calculation serves as input for valence and core level BSE calculations. For non-equilibrium studies, a RT-TDDFT calculation is performed after the DFT step to obtain the time-dependent electronic occupations. These are then used as input for the subsequent BSE calculations. The BSE results build the basis for multiple BRIXS calculations for different combinations of polarization of the incoming and outgoing light. The final RIXS spectra for all polarization combination or is obtained as an average over them.

The results of the BSE calculations, specifically the eigenvalues E^λ and eigenvectors $A_{ij\mathbf{k}}^\lambda$, serve as input for BRIXS, which enables the simulation of RIXS spectra for arbitrary combinations of incoming and outgoing light polarizations to cope with the experimental setup. For each polarization configuration, all contributing scattering pathways $t^{(1)}$, $t^{(2)}$ and $t^{(3)}(\omega_1)$ are evaluated for a fixed set of excitation energies ω_1 . Subsequently, the RIXS double differential cross sections (DDCS) are calculated using pyBRIXS. If multiple polarization channels contribute equally in the experiment, the average of the RIXS cross sections can be calculated before visualizing the final results.

4 RIXS in graphite

Graphite is a well-studied material with a versatile application range. It is a prototypical layered material with a hexagonal crystal structure composed of stacked graphene sheets. The combination of strong in-plane covalent bonding and weak inter-layer van der Waals interactions results in semi metallic electronic properties. These characteristics make graphite an ideal system for studying fundamental excitations in solids. Also, due to its simplicity, availability, and well-characterized nature, graphite has been widely investigated both experimentally and theoretically. Nonetheless, graphite continues to be of interest in advanced spectroscopic studies. In this work, we apply the *ab initio* approach to RIXS, introduced in the previous sections and compare it to experimental data obtained in a collaboration with Marco Malvestuto.

4.1 Structural properties of graphite

Graphite crystallizes in a layered structure with hexagonal symmetry. Each layer consists of carbon atoms arranged in a two-dimensional honeycomb lattice, where each atom is sp^2 -hybridized and forms strong covalent σ bonds with its three nearest neighbors. Delocalized π bonds extend perpendicular to the plane, dominating the electronic properties of the material. In graphite, the single graphene layers are stacked in an AB configuration, in which every second layer is laterally shifted by a vector of $\frac{1}{3}\mathbf{a}_1 + \frac{2}{3}\mathbf{a}_2$. The primitive unit cell of graphite is defined by the lattice vectors

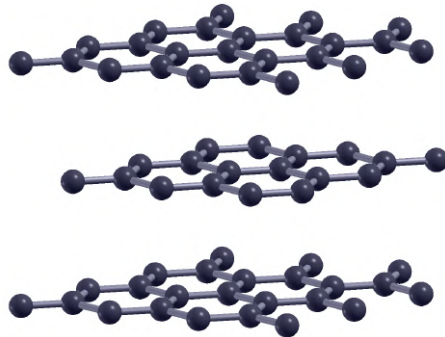


Figure: Crystal structure of graphite, consisting of stacked graphene layers in an AB configuration.

$$\mathbf{a}_1 = \left(\frac{1}{2}a, \frac{\sqrt{3}}{2}a, 0 \right), \quad \mathbf{a}_2 = \left(\frac{1}{2}a, -\frac{\sqrt{3}}{2}a, 0 \right), \quad \mathbf{a}_3 = \left(0, 0, c \right), \quad (4.1)$$

with lattice parameters $a = 2.461 \text{ \AA}$ and $c = 6.708 \text{ \AA}$ [65]. The primitive unit cell contains 4 atoms in

$$\begin{aligned} \mathbf{R}_1 &= \mathbf{a}_1, & \mathbf{R}_2 &= \frac{2}{3}\mathbf{a}_1 + \frac{1}{3}\mathbf{a}_2, \\ \mathbf{R}_3 &= \frac{2}{3}\mathbf{a}_1 + \frac{1}{3}\mathbf{a}_2 + \frac{1}{2}\mathbf{a}_3, & \mathbf{R}_4 &= \frac{1}{3}\mathbf{a}_1 + \frac{2}{3}\mathbf{a}_2 + \frac{1}{2}\mathbf{a}_3. \end{aligned} \quad (4.2)$$

Early RIXS investigations on graphite by Carlisle et al. [14] focused on experimental spectra at the carbon K-edge and their interpretation in terms of projected band structures. Theoretical modeling at that time primarily relied on the independent particle approximation (IPA), which already reproduced key spectral features [15]. Shirley et al. later confirmed that, due to the delocalized nature of the involved states, electron-hole interactions modify the spectral shape only weakly [16, 17].

Although IPA based calculations already reproduce main RIXS features, BSE based approaches provide a more complete and accurate treatment. Later studies by Zhang et al. also revealed excitonic effects in graphene [18] and suggest the necessity of including them also in RIXS calculations for graphite.

4.2 Experimental work

Based on his experimental results carried out at the Elettra Synchrotron in Trieste [22], Marco Malvestuto invited us to collaborate on this topic. RIXS measurements were done for highly oriented pyrolytic graphite (HOPG), which was cleaved in air before the experiment. This way, the experiment could be performed on a single, pure crystal with a clean and bulk-like surface. Furthermore, the sample was oriented such that the graphene layers lay parallel to the x - y plane of the experimental setup. The experimental setup is shown in Fig. 6. For different incident beam angles of 30° and 59° , the system was probed by a free electron laser (FEL) emitting X-ray photons with a constant polarization p_{in} fixed in the x - z plane. The scattered photons were detected at a fixed scattering angle of 90° with respect to the incoming beam. In contrast to the incoming beam, the polarization of the outgoing photons does not follow any selection rules and is not detected by the spectrometer. The incident photon energy was tuned to the carbon K-edge, around 284 eV, with an instrumental resolution of 35 meV. A core-hole lifetime of 7-10 fs was estimated in accordance with [66, 67].

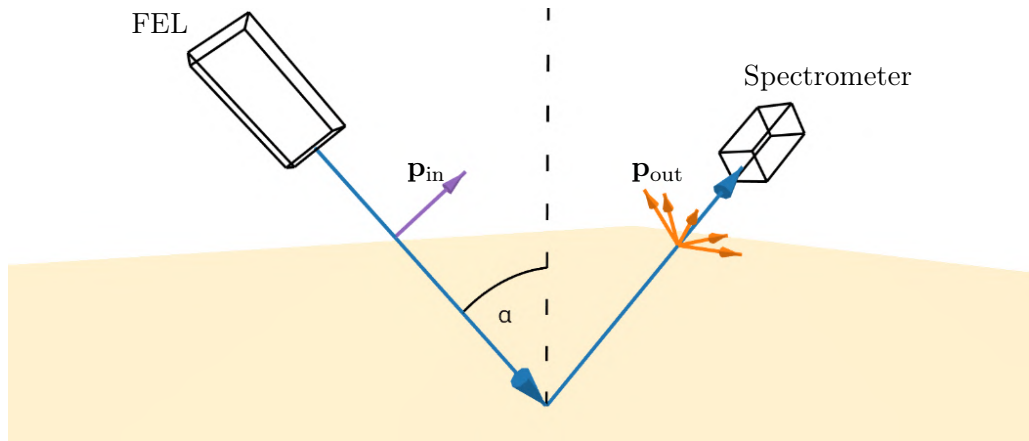


Figure 6: Experimental setup: An FEL laser with fixed polarization is focused onto a sample at an angle α . The emitted photons are detected by a spectrometer positioned perpendicular to the incident beam direction.

The experiment does not only probe static graphite, but also aims to investigate whether an ultrafast modification of the core-hole exciton screening in graphite can be induced and observed. To this end, time-resolved RIXS measurements were performed on both unpumped (equilibrium) and pumped (non-equilibrium) graphite. In the time-resolved setup, graphite is first excited by a short laser pulse in the near UV range (wavelength of 266 nm), which populates specific valence and conduction states. The excitation is tuned to address electronic transition near the M saddle point in the band structure, particularly the $1s - 2p_\pi$ transition in the out-of-plane direction. This ultrafast excitation creates a transient, non-equilibrium electronic state, and RIXS spectra taken shortly after the pump allow us to study how the screening of the core hole is modified on ultrashort time scales. The pulse with a duration of 45 fs creates a pump fluence of 30 mJ/cm^2 on the sample. After delay times of up to 1 ps RIXS spectra are measured for either fixed incoming photon energy ω_1 or for a fixed delay time Δt .

4.3 Electronic structure

First, we consider the underlying ground state properties of graphite, for which a structural relaxation was performed. Due to the weak interlayer binding, van der Waals interactions play a crucial role and must be properly treated. The Tkatchenko-Scheffler van der Waals

correction [68] was applied in order to treat inter-plane interactions. DFT ground state calculations were performed using the GGA-PBE xc-functional, a plane-wave cutoff of $\text{rgkmax}=8$, and a $24 \times 24 \times 9$ \mathbf{k} -grid. An analysis of the density of states (DOS) and the band structure, which are both in excellent agreement with literature [69–71], is provided in Fig. 7.

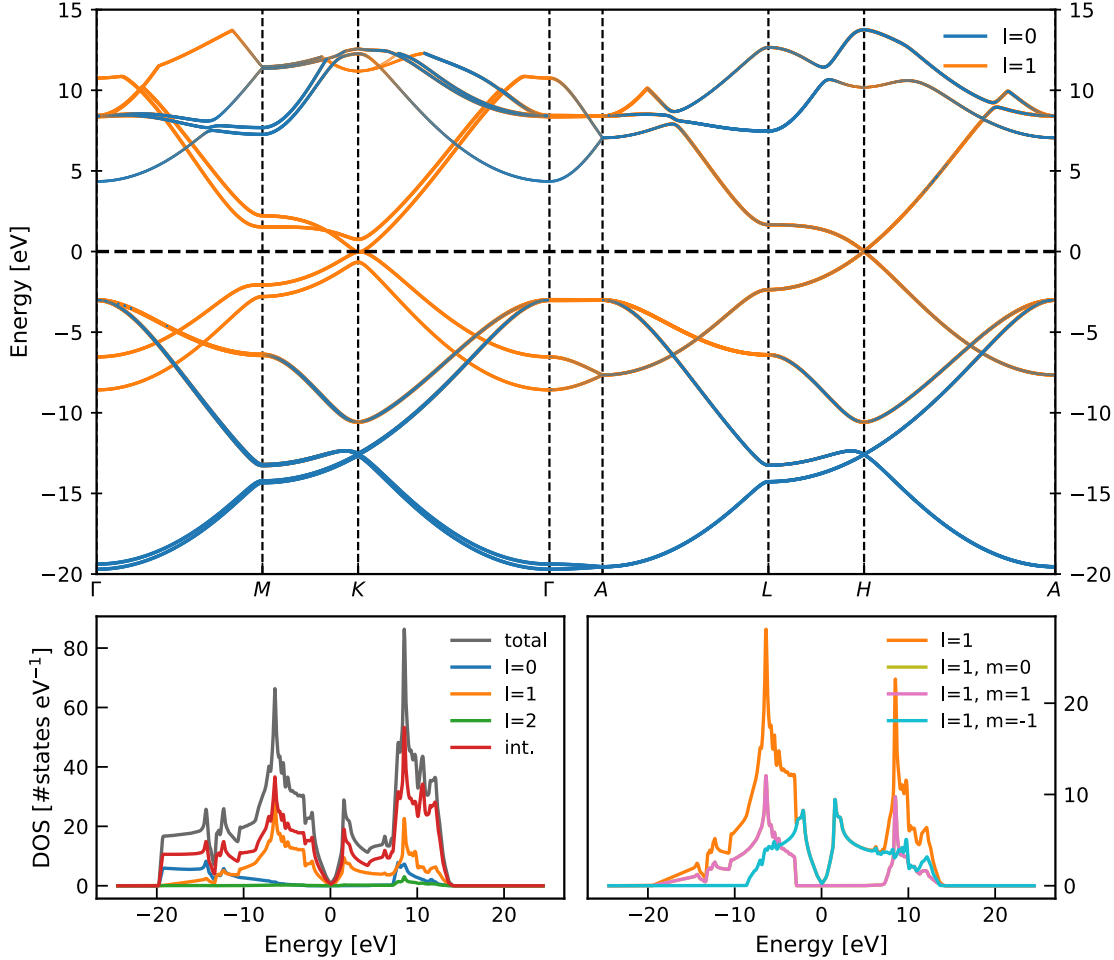


Figure 7: The orbital-projected band structure of graphite is shown in the top panel, indicating s -states ($l = 0$) and p -states ($l = 1$). The corresponding orbital-projected density of states is displayed on the bottom left, resolved by angular momentum channels (l) and the interstitial region, and on the bottom right for $l = 1$, further resolved by the magnetic quantum number m .

Near the Fermi energy, mainly $l = 1$ contribute to the electronic structure due to the delocalized π -orbitals oriented perpendicular to the layers. Especially near the M -point, the region in which the pumping is supposed to influence the p_π orbitals, they in fact provide the largest contributions. In contrast, for energies away from the Fermi energy, in-plane electronic states in form of s -orbitals predominate. For other high-symmetry points such as Γ and H , however, a mixture of the two contributions is present. This obviously also shows up in the density of states. In addition we provide a more detailed analysis of $l = 1$ channel in form of the m -projected DOS and observe high impact in the Fermi energy region only for $m = -1$, i.e., the out-of-plane direction.

For graphite, a semi-metallic material with strong screening and the absence of a band gap, quasi-particle corrections from more expensive methods such as GW are, in princi-

ple, available and can lead to self-energy shifts, especially in the conduction band region. But for core level excitations, existing *GW*-based models are insufficient. Since the main spectral features relevant for this study are expected to be qualitatively captured at the DFT level, this work relies on DFT input.

4.4 Spectroscopy in graphite

In order to perform the RIXS calculations, the underlying BSE calculations for optical and X-ray absorption have to be carried out. Taking the PBE results as a basis, BSE calculations were performed on $12 \times 12 \times 4$ **k**-grid with a plane-wave cutoff of 3.5.

4.4.1 Optical spectra

We present the optical spectra in terms of the in-plane (ϵ_{xx}) and out-of-plane (ϵ_{zz}) components of the imaginary part of the dielectric tensor ϵ_M in Fig. 8. $N_v = 8$ valence states, corresponding to the number of (partially) occupied states in the ground state, and $N_c = 15$ conduction states were considered. A Gaussian broadening of 0.49 eV was applied for all calculated spectra. For comparison, we show the results obtained within the independent-particle approximation.

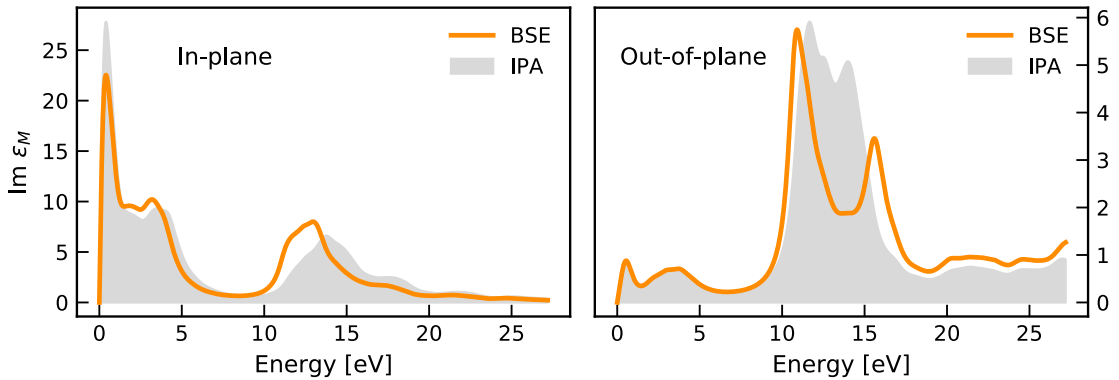


Figure 8: Optical absorption spectra of graphite obtained from singlet BSE (orange line) and within the IPA (grey shaded area) for in-plane (left) and out-of-plane (right) polarization.

While for the in-plane components, as expected, screening effects play a major role and thus the main features already occur on the independent-particle level, for the out-of-plane direction, excitonic effects are inevitable, showing up in the splitting of the second peak in the 10-15 eV region. Comparison with literature (Fig. 9) shows excellent agreement with other calculations and experiments.

The in-plane spectrum has two main peaks. The one in the low energy region < 5 eV is due to $\sigma \rightarrow \sigma^*$ and $\pi \rightarrow \pi^*$ interband transitions [11]. Especially the peak in the range of 4 eV originates from $\pi \rightarrow \pi^*$ transitions near the M -point and the L -point, and therefore exactly the high-symmetry points where the pumping should take place. The second main feature in the > 10 eV region originates from $\sigma \rightarrow \sigma^*$ transitions near the M -, Γ - and L -points [11]. These are associated with transitions within the in-plane bonding and antibonding σ -bands and are already well captured at the independent-particle level.

The out-of-plane spectra has two main features. The low-energy range is characterized by a weak peak induced by inter-layer transitions. The second major feature appears in the 10–15 eV range and stems from $\pi \rightarrow \sigma^*$ and $\sigma \rightarrow \pi^*$ transitions across layers [72]. Notably,

this region is also where excitonic effects become crucial, leading to the above-mentioned splitting.

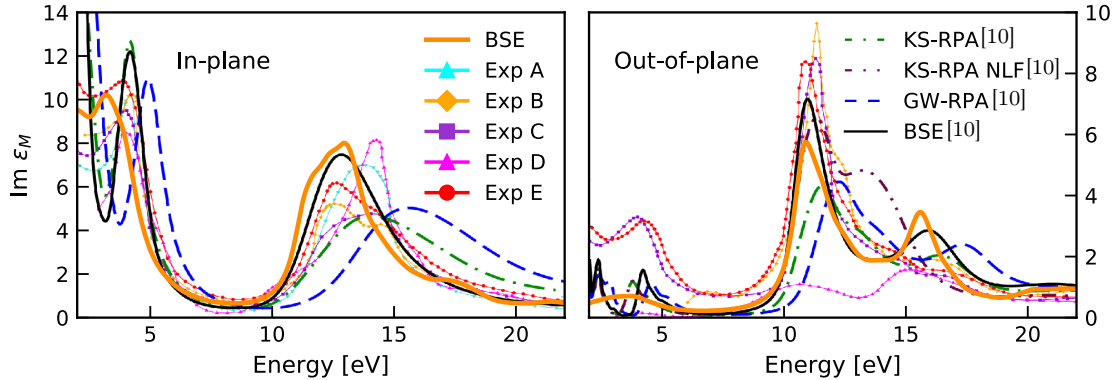


Figure 9: Optical spectra of graphite for in-plane (left) and out-of-plane (right) polarization obtained from BSE. Comparison with theoretical results from [10] for BSE, GW-RPA, and KS-RPA with and without local field effects. Experimental data taken from Ref. [73] (A), Ref. [74] (B), Ref. [75] (C), Ref. [76] (D), and Ref. [77] (E).

4.4.2 K -edge spectra

For the carbon K -edge core level absorption, a scissors shift of 18.5 eV was applied in the BSE calculations to align the first peak with experimental data. These BSE calculations were performed considering $N_c = 40$ conduction bands.

Instead of showing the pure in-plane and out-of-plane components, both exhibiting one sharp peak, we want to address the different measuring angles in experiment and the role they play for the spectra. The components mix according to $S_{\text{tot}}(\alpha) = \cos^2(\alpha)S_{x-y} + \sin^2(\alpha)S_z$. In Fig. 10, we display the K -edge excitation spectra for $\alpha = 30^\circ$ and $\alpha = 59^\circ$. In addition, results obtained in the independent-particle approximation are shown (using the same scissors shift as for BSE).

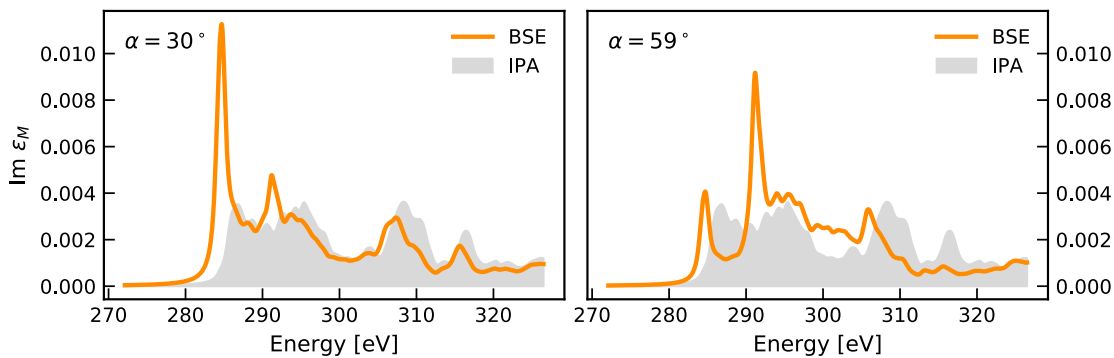


Figure 10: Carbon K -edge core level absorption spectra for graphite for incident beam angles $\alpha = 30^\circ$ and $\alpha = 59^\circ$.

While for $\alpha = 30^\circ$, the first peak at ~ 284 eV originating from the polarization perpendicular to the plane is dominant, the second peak at ~ 292 eV, stemming from the in-plane component, is suppressed. For $\alpha = 59^\circ$, however, both cartesian components impact the spectra. The characteristic peak structure arises only when excitonic effects are included, indicating their central role in the spectrum, even though screening tends to diminish excitonic interactions. These findings are overall consistent with experimental results and

literature data [12, 13], although Olovsson et al. [78] report a noticeable influence of lattice vibrations, which are not accounted for in the present calculations.

In the RIXS process, we will probe on energies of approximately 284–286 eV and therefore only map the first peak, which aligns with the experimental results.

4.5 RIXS calculations for graphite

Results for the carbon K-edge RIXS spectra are obtained for incoming photon angles of 30° and 59° using BRIXS and presented in Fig. 11. In order to compare with experiment, described in Chapter 4.2, the new implementations within the BRIXS code are used.

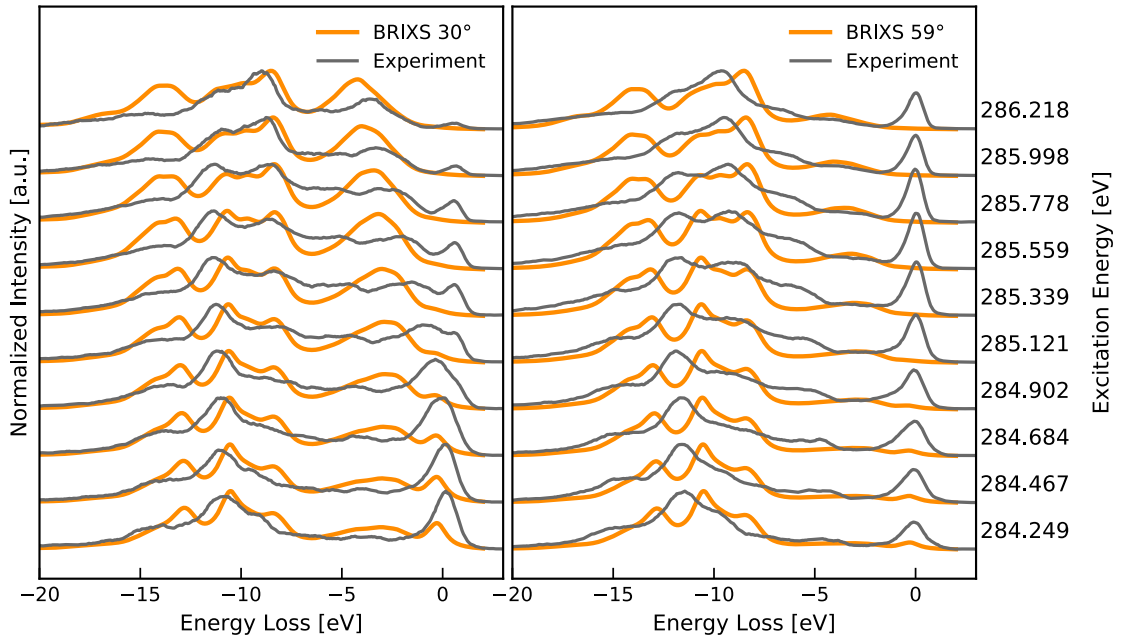


Figure 11: RIXS spectra for the carbon K-edge of graphite for incident angles of 30° and 59° for varying energies ω_1 compared to experiment; BRIXS calculations in orange and experimental results in gray.

While the polarization of the incoming photon is fixed in the x-z-plane, the polarization of the outgoing photon is varied, depending on the angle α as $\mathbf{p}_{\text{in}} = (\cos \alpha, 0, \sin \alpha)$, leaving one degree of freedom undetermined. Due to symmetry, it is sufficient to consider polarizations in a 90° range between the two extrema, i.e., $\mathbf{p}_{\text{out},1} = (-\sin \alpha, 0, \cos \alpha)$, and $\mathbf{p}_{\text{out},2} = (0, 1, 0)$.

In total, RIXS calculations for nine outgoing polarizations were performed. Subsequently the average over them was taken on the level of the RIXS DDCS, to approximate the angular average of the emitted intensity over all polarization directions as present in the experimental setup. A lifetime broadening of 0.5 eV was applied for the intermediate state, in order to match with experimental resolution [79].

In Fig. 12 we compare RIXS spectra obtained from BSE calculations to those obtained from IPA results. As for the spectra discussed in Chapter 4.4, we recognize major differences between them, which again confirms the need to include excitonic effects.

For both incident angles, the main spectral features show very good agreement with experiment. While the energetic positions of the dominant peaks hardly differ between the two experimental setups, notable differences arise in their relative intensities. At a scat-

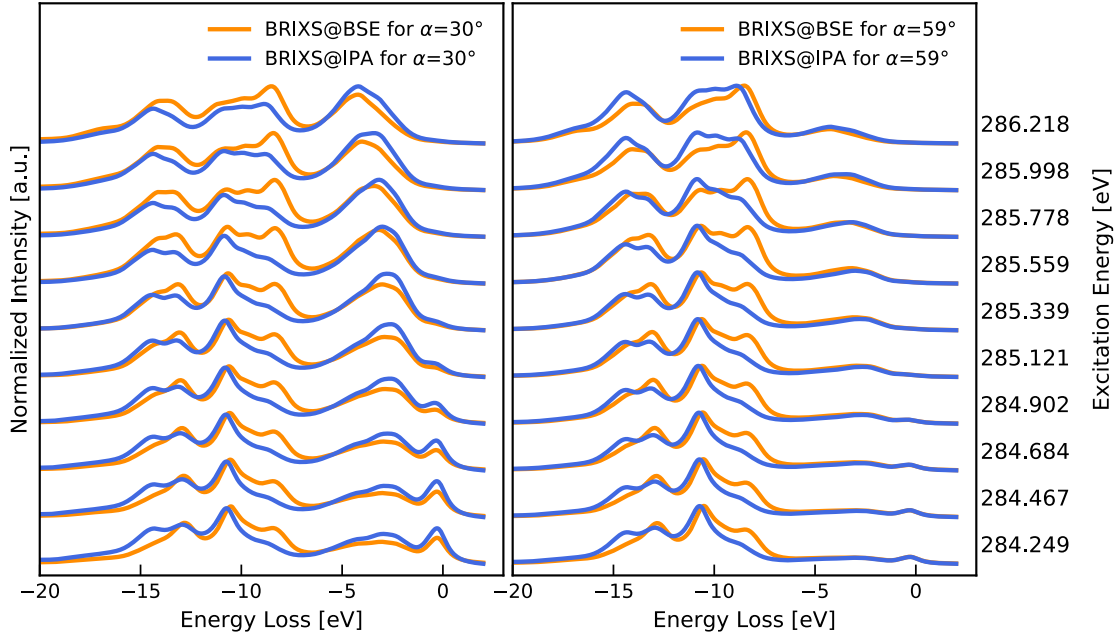


Figure 12: RIXS spectra for the carbon K-edge of graphite for incident angles of 30° and 59° for varying energies ω_1 from singlet BSE in orange and IPA in blue.

tering angle of $\alpha = 30^\circ$, the polarization vector of the incoming X-ray is predominantly oriented parallel to the graphene planes, favoring transitions into π^* states. In contrast, at $\alpha = 59^\circ$, the electric field has a stronger out-of-plane component, enhancing transitions into σ^* states. These differences are already captured within the underlying BSE calculations and are consistently reflected also in the RIXS spectra. Beyond these angular dependencies, the individual spectral features reveal insights into the underlying electronic structure. In the following, we discuss them in terms of their energetic position, orbital character, and excitation-energy dependence, closely based on discussions by Carlisle et al. [14, 15] in combination with the orbital projected band structure presented in Fig. 7.

The dominant spectral structure lies between 8 and 15 eV energy loss and appears consistently across both experimental setups. These features originate from overlapping contributions from multiple $\sigma \rightarrow \sigma^*$ transitions near the M - and L -points. Their position shifts with the incident photon energy, reflecting the dispersion of the underlying band structure. At lower excitation energies the peak near 11 eV is dominant, corresponding to de-excitations from deeper valence σ -states. In contrast, as the excitation energy increases, the spectral weight shifts towards a peak around 8 eV, which involves transitions from higher lying, less bound σ -states. In comparison to experimental data, this peak region shows a constant shift towards lower energy-loss values.

At higher energy-loss energies, above 15 eV energy loss, a broader σ -band based feature is arising with higher excitation energies. This is associated with deep-lying σ -states near the M -point and already shows up on IPA level. In contrast to the features around 8 and 11 eV, the energy loss shifts with increasing excitation energy, which reflects the downward dispersion of the conduction band near the corresponding states. The fine structure of this peak is not resolved in experiment even though the broad shoulder ranges up to 20 eV. Similar results were reported by Zhang et al. [18] for graphene, where such a feature was absent in the measured spectrum despite its theoretical prediction. A possible explanation, proposed by the experimentalists [M. Malvestuto, private communication], is self-absorption, i.e., the re-absorption of emitted photons within the sample itself, which

can suppress or distort spectral features, particularly in energy regions of strong absorption or under certain experimental setups

Unlike the σ -related features, which appear independent of the incident angle, due to the more isotropic character of the σ -orbitals, $\pi \rightarrow \pi^*$ transitions are more prominent for $\alpha = 30^\circ$, consistent with experimental observations. The increased intensity is attributed to the polarization vector being oriented more parallel to the graphene planes, thereby enhancing the coupling to out-of-plane π -orbitals.

Although not dominant, a weak feature appears around 1 eV originating from transitions near the K -point, which are symmetry-forbidden in graphene and become visible due to interlayer coupling. Beyond that, the experimental elastic peak around 0 eV energy loss is not covered in the theoretical results, since only coherent effects are considered within BRIXS.

The most intense π -state contribution to the spectra emerges in the mid-loss region of 3-7 eV, which is attributed to transitions mainly around the M saddle-point, but also near the K -point. As the excitation energy increases, the feature shifts towards higher energy loss, reflecting the π -band dispersion near the Fermi energy and subsequent transitions into deeper valence bands.

While the present theoretical approach captures many spectral features and angular dependencies observed in experiment, the current calculations do not account for electron-phonon or exciton-phonon interactions. Including such effects, either statically or within a time-dependent framework, could yield a more comprehensive understanding of the interplay of lattice vibrations and electronic excitations, thereby enhancing the interpretation of RIXS spectra. Experimental evidence for the sensitivity of carbon K -edge RIXS to electron-phonon coupling has been reported by Dashwood et al. [19], who observed vibrational fine structure in the σ^* region. This endorses the potential relevance of electron-phonon coupling, particularly in the high-energy loss regime, and motivates future theoretical extensions beyond the purely electronic description adopted here.

4.6 Non-equilibrium spectroscopy in graphite

As introduced in Chapter 4.2, the experimental setup aims to perform time-resolved RIXS (tr-RIXS) measurements on optically excited graphite. In this pump-probe scheme, the femtosecond laser pulse of a wavelength of 266 nm is used to selectively excite electrons near the M saddle point. From a theoretical point of view, simulating these processes requires going beyond the so far used methods.

In order to simulate this non-equilibrium electronic system from first principles, real-time time-dependent density functional theory (RT-TDDFT) is employed, to propagate the KS system in time, starting from the ground state. An external perturbation is mimicking the effect of the pump laser. For each incident beam angle, a separate RT-TDDFT calculation is necessary. The pump-induced changes in the occupation numbers are then extracted and used as input for subsequent BSE and RIXS calculations. This approach does not yet include the full time evolution of the two-particle Green's functions, but it allows a physically motivated description of the optically excited system, as experimental parameters such as delay-time, pump energy, pump fluence, and pump length can directly be considered. It should be noted, however, that in RT-TDDFT based BSE calculations only the modified electronic occupations are used, while the underlying Kohn-Sham energies and wavefunctions remain unchanged.

Taking the occupation numbers for a delay time of 150 fs between pump and RIXS measurement from RT-TDDFT, optical and core level excitation spectra can be calculated

within the BSE framework as described in Sec. 2.4. In Fig. 13, we present in-plane and out-of-plane optical spectra for incident angles of 30° and 59° as well as the difference to the equilibrium case.

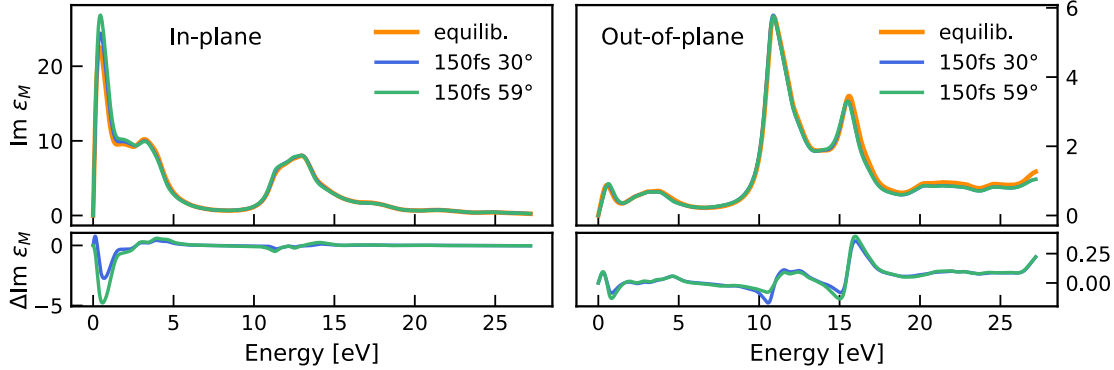


Figure 13: Top: Optical absorption spectra from singlet BSE for non-equilibrium graphite, obtained by pumping for 45 fs with a 266 nm laser and a delay time of 150 fs for in-plane (left) and out-of-plane (right) polarization. Bottom: Differences to equilibrium results.

The optical absorption spectra exhibit only subtle changes compared to those of the equilibrium system. For the in-plane polarization, noticeable differences already emerge at the independent-particle (IP) level in the low-energy region, while excitonic effects lead to additional minor deviations in the second peak region. For out-of-plane polarization, compared to the equilibrium system spectra, only small differences appear above 15 eV, primarily due to excitonic effects. These same behavior is observed in the core-level excitations. In Fig. 14 X-ray absorption spectra for pumped graphite are displayed, again as a combination of in-plane and out-of-plane components as a function of the incident beam angle.

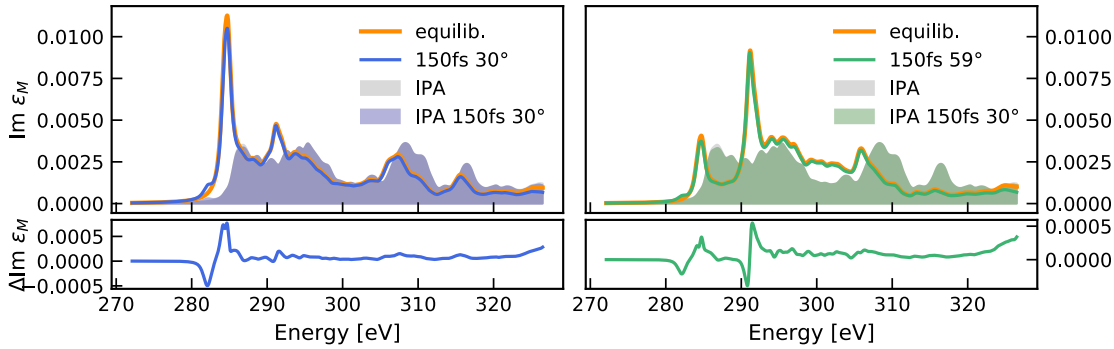


Figure 14: Top: Carbon K-edge spectra from singlet BSE for non-equilibrium graphite, obtained by pumping for 45 fs with a 266 nm laser and a delay time of 150 fs for incident beam angles of 30° (left) and 59° (right). Bottom: Differences to equilibrium results.

For both incident angles of 30° and 59° only subtle differences are present in comparison to the equilibrium spectra. An additional minor peak occurs at an energy slightly below the first absorption edge, while the peak intensity of the in-plane K-edge is lowered. However, given the experimental range of excitation energies, this additional peak will not feature in pumped RIXS results and thus could be a starting point for future research.

4.7 RIXS for non-equilibrium graphite

After comparing the optical and core-level absorption spectra of optically excited graphite to those of the equilibrium case, we now focus on the analysis of pump-induced modifications on the level of RIXS spectra. We calculated RIXS spectra for incident angles of 30° and 59° at a pump-probe delay time of 150 fs. Comparison to experimental results are displayed in Fig. 15. As for the static case, we use a total lifetime broadening of 0.5 eV in order to match the experimental resolution. While the overall agreement remains good, the experimental spectra exhibit significant noise, limiting direct comparisons. Still, several trends are identifiable by comparing pumped and unpumped graphite results and in comparison with experimental data.

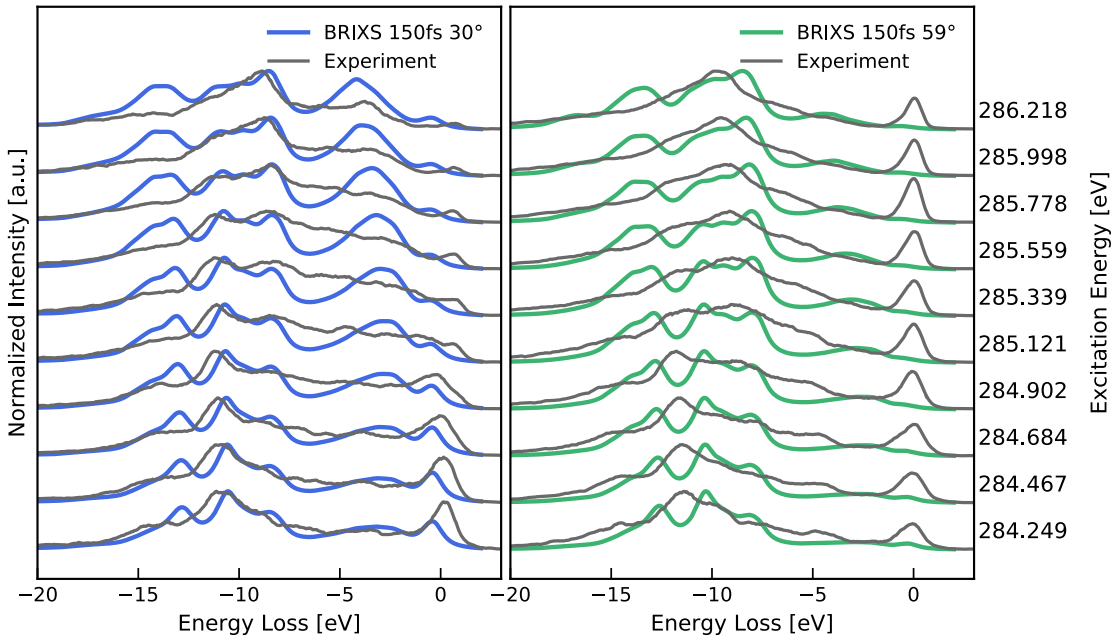


Figure 15: Non-equilibrium RIXS spectra for the carbon K-edge of graphite, obtained by pumping for 45 fs with a 266 nm laser and a delay time of 150 fs, for incident angles of 30° and 59° and different excitation energies ω_1 ; BSE based BRIXS calculation in blue/green, experimental results in gray.

In general, the spectra of the pumped system exhibit quite similar features as those of the equilibrium configuration and the observed spectral changes due to the optical excitation are subtle. No new spectral features or systematic energy shifts are observed. For an incidence angle of $\alpha = 30^\circ$, only a slight shift towards higher loss energies is observed, while for $\alpha = 59^\circ$, additionally weak modulations in selected energy ranges appear. Notably, while for low excitation energies the spectra do align, at higher excitation energies, the first inelastic peak around 7.5 eV shows a stronger intensity compared to the equilibrium case, which may indicate a redistribution of occupations or modified transition probabilities caused by the excitation.

For 30° , the calculated non-equilibrium spectra reproduce experimental features well up to an energy loss of 12 eV, including a persistent shift in the 7-15 eV region, which appears considerably less pronounced than in equilibrium. At higher energy losses, theory predicts an additional excitation feature at high excitation energies that is not clearly visible in the experiment, but was already visible on the equilibrium level. As discussed for the equilibrium case, they correspond to transitions from deep-lying σ -states, which are not affected by the pumping process.

For 59° , due to the isotropic character of the σ -orbitals, these high loss energy feature also appear. However, also the experimental data show small intensity such that the difference between both is less pronounced. In contrast to the 30° case, the persistent shift, compared to experiment, for energy loss values of 7-15 eV appears slightly higher for this incidence beam angle. Additionally, peaks in the 3-7 eV region arising from π -orbital driven transitions, are more strongly pronounced in comparison to the σ driven peaks. In the experimental results, this feature only becomes prominent for excitation energies above 286 eV, while at lower excitation energies it is suppressed by an increasing background signal in the energy loss range of 1–9 eV.

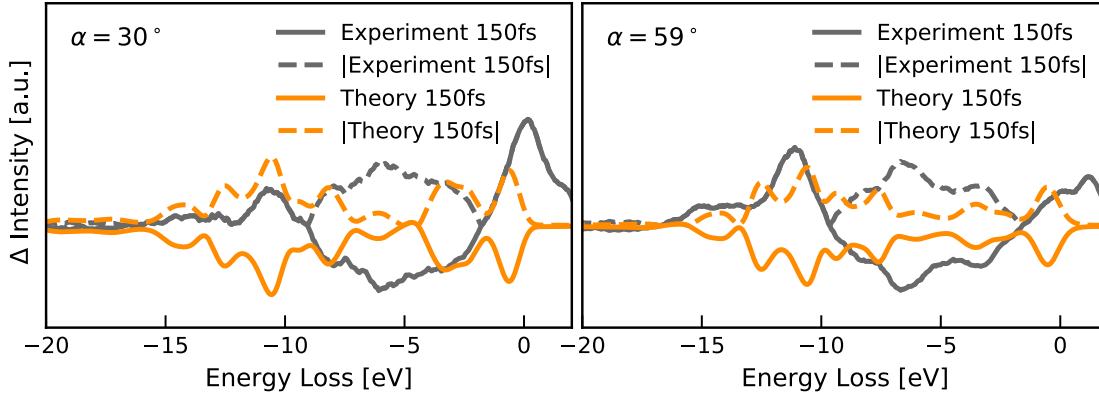


Figure 16: Difference between equilibrium and non-equilibrium RIXS spectra for the carbon K-edge of graphite, obtained by pumping for 45 fs with a 266 nm laser and a delay time of $\Delta t = 150$ fs. Summed over all incident excitation energies ω_1 . Theoretical results in orange and experimental results in gray. Corresponding absolute differences are indicated by dotted lines.

In Fig. 16 we display the difference of equilibrium and non-equilibrium spectra, summed over all considered excitation energies ω_1 , for both incident beam angles α . Since differences appear in the direction of the changes, both the pure difference of theoretical results and their corresponding absolute values are displayed. Notably, specially in the energy loss region of 7-12 eV, corresponding to the second main feature observed in prior RIXS spectra, the spectral positions match with the experimental findings. Overall, although differences appear in the direction of the changes, in their absolute values experimental and theoretical results show general agreement. Pumping induced differences and their spectral position are reproduced in reasonable agreement, but leave room for improvement.

Up to now, all time-dependent results were calculated for a fixed pump-probe delay time of 150 fs, while varying the excitation energy ω_1 within the experimental energy range. Still, from an experimental perspective, it is often more feasible to keep the excitation energy fixed and measure RIXS spectra as a function of pump-probe delay time. On the theoretical side, however, this approach is significantly more demanding, as each delay time and incident angle requires a repetition of the complete workflow including RT-DDFT pumping simulations, BSE-, and RIXS calculations. Figure 17 shows the resulting RIXS spectra for delay times Δt ranging from 100 fs to 300 fs at fixed excitation energies $\omega_1 = 285.02$ eV and $\omega_1 = 285.57$ eV.

For short delay times ($\Delta t = 100$ fs), the spectra still appear to be close to their equilibrium counterparts, indicating that the system is still in the early phase of responding to the pump excitation. At intermediate delays around 150–250fs, deviations from the equilibrium case become visible, especially for the incident angle of $\alpha = 59^\circ$, reflecting the transient non-

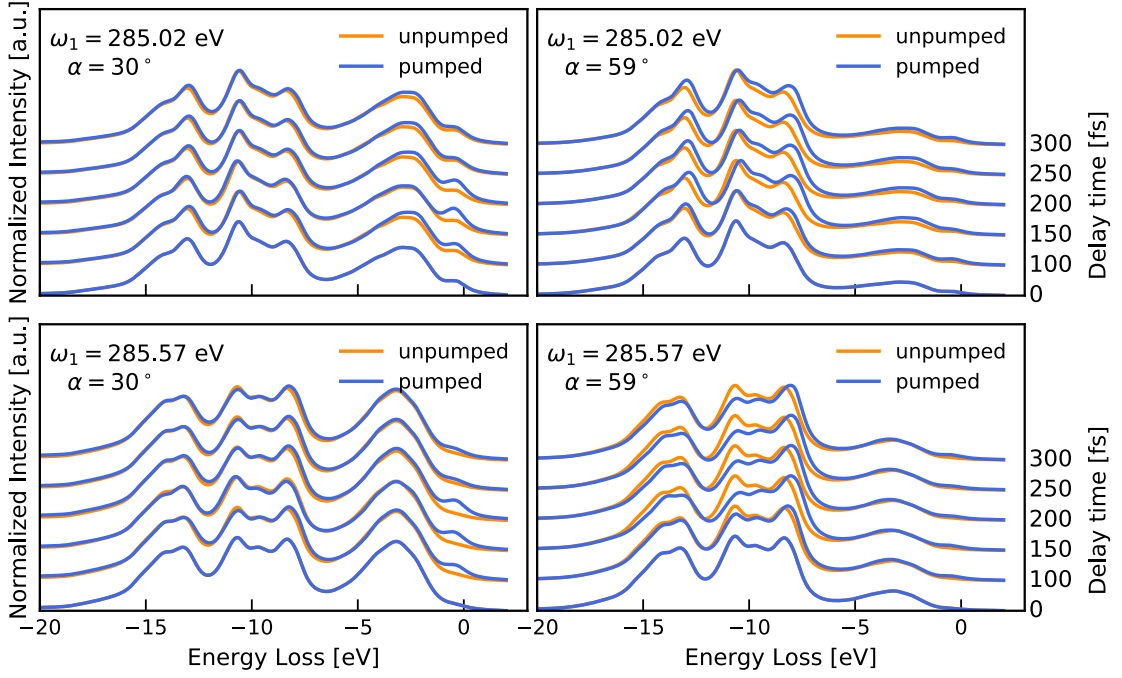


Figure 17: Non-equilibrium RIXS spectra for the carbon K-edge of graphite, obtained by pumping for 45 fs with a 266 nm laser and excitation energies $\omega_1 = 285.02$ eV and $\omega_1 = 285.57$ eV, for incident angles of 30° and 59° and different delay times Δt ; equilibrium spectra in orange and non-equilibrium spectra in blue

equilibrium electronic structure. For delay times higher than 250 fs, the spectra begin to resemble the equilibrium ones again, suggesting a partial electronic relaxation.

Generally, the extent of these spectral modifications depends sensitively on the incident angle and excitation energy. For an incident angle of 30° , the deviations between the spectra corresponding to pumped and unpumped graphite are relatively small and confined to the low energy loss region (< 5 eV). In contrast, for $\alpha = 59^\circ$, the spectra exhibit stronger changes, particularly at $\omega_1 = 285.57$ eV, where pronounced differences in the 7-11 eV energy loss region are observed.

5 Conclusions and Outlook

In this work we presented *ab-initio* time-resolved RIXS calculations in graphite for different incident beam angles. The aim was to capture polarization-dependent spectral features arising from excitations across the carbon K-edge, both in equilibrium and after additional optical excitation, in graphite, a material with strongly anisotropic electronic structure. We used an existing formalism for computing RIXS spectra based on the BSE and adapted it to account for an arbitrary choice of polarization vectors of incoming and outgoing light.

Starting from DFT ground state calculations for graphite, we solved the BSE to obtain both optical and carbon K-edge core-level absorption spectra. These served as basis for computing RIXS spectra for graphite. By explicitly incorporating the polarization vectors of incoming and outgoing photons as well as varying the incident beam angle, we were able to reproduce key features of the underlying experimental setup and obtain theoretical RIXS spectra that reproduce main spectral features found in experimental observations.

Furthermore, to study time-dependent non-equilibrium effects, we investigated optically pumped graphite. RT-TDDFT was employed to account the pump process, propagate the KS system in time, and calculate the non-equilibrium occupations. Subsequently, the resulting excited-state properties were incorporated into the BSE-based RIXS workflow to compute the corresponding time-resolved RIXS spectra. Obtained results showed good agreement with experimental findings.

Despite the overall good agreement between theory and experiment, there is room for improvement. To account for this, our work could be extended in several directions. A first step could be incorporating quasi-particle corrections in the underlying electronic structure via the *GW*-approximation. *GW* based BSE calculations could improve the RIXS spectra particularly in the relative distance of spectral features. Second, especially relevant for long pump-probe delay times, RT-TDDFT methods could be extended beyond the occupation number representation, by incorporating Kohn-Sham energies and states of the propagated system into the subsequent BSE calculations.

Moreover, including both electron-phonon and exciton-phonon coupling, could improve the description of energy shifts, particularly in core level absorption calculations. These interactions are especially relevant at longer time delays, where effects of lattice dynamics and vibronic effects increase. Their inclusion would thus provide a more comprehensive understanding of the interplay between lattice vibrations and electronic excitations, thereby enhancing the interpretation of experimental RIXS.

Finally, our methodology is applicable to a broader class of materials. For example, preliminary experimental work for Li-doped graphite is currently carried out by our collaborator Marco Malvestuto, aiming to probe how charge doping modifies the excitation spectrum of graphite. From a theoretical perspective, describing such systems requires careful consideration of the doping-induced changes in the electronic structure, including enhanced screening, band filling, and potential symmetry breaking due to lithium intercalation. The workflow presented in this thesis can be directly applied for dealing with such systems.

A Appendix

A.1 2nd Quantization

In the following we derive one of the main quantities of MBPT, the Hamiltonian using the second quantization formalism, and adopt the occupation number representation. We follow close to the derivations provided in Refs. [23, 40, 41]. In this representation, the many-body Hamiltonian is described by

$$\hat{H} = \int d^3r \hat{\psi}^\dagger(\mathbf{r}) h(\mathbf{r}) \hat{\psi}(\mathbf{r}) + \frac{1}{2} \int d^3r \int d^3r' \hat{\psi}^\dagger(\mathbf{r}) \hat{\psi}^\dagger(\mathbf{r}') v_c(\mathbf{r}, \mathbf{r}') \hat{\psi}(\mathbf{r}') \hat{\psi}(\mathbf{r}), \quad (\text{A.1})$$

where $h(\mathbf{r}) = -\frac{1}{2}\nabla^2 + V(\mathbf{r})$ is the single electron Hamiltonian, and $v_c = \frac{1}{|\mathbf{r}-\mathbf{r}'|}$ represents the Coulomb interaction.

The fermionic field operators $\hat{\psi}^\dagger(\mathbf{r})$ and $\hat{\psi}(\mathbf{r})$, which create and annihilate particles at \mathbf{r} , satisfy the anti-commutation relations

$$\left[\hat{\psi}^\dagger(\mathbf{r}), \hat{\psi}^\dagger(\mathbf{r}') \right]_+ = \left[\hat{\psi}(\mathbf{r}), \hat{\psi}(\mathbf{r}') \right]_+ = 0, \quad \text{and} \quad \left[\hat{\psi}(\mathbf{r}), \hat{\psi}^\dagger(\mathbf{r}') \right]_+ = \delta(\mathbf{r} - \mathbf{r}'). \quad (\text{A.2})$$

The time evolution of the system in the Heisenberg picture given by

$$\psi(\mathbf{r}, t) = e^{iHt} \psi(\mathbf{r}) e^{-iHt}, \quad (\text{A.3})$$

is described by the Heisenberg equation of motion for the field operators

$$i \frac{\partial}{\partial t} \hat{\psi}(\mathbf{r}, t) = \left[\hat{\psi}(\mathbf{r}, t), \hat{H} \right] = \left[h(\mathbf{r}) + \int d^3r' v_c(\mathbf{r}, \mathbf{r}') \hat{\psi}^\dagger(\mathbf{r}', t) \hat{\psi}(\mathbf{r}', t) \right] \hat{\psi}(\mathbf{r}, t). \quad (\text{A.4})$$

Since this equation is a complicated, non-linear expression in terms of field operators, a direct solution is not feasible, necessitating the use of perturbative methods [40].

A.2 Derivation of the BSE

The detailed derivation of the Bethe-Salpeter equation using Green's function methods are presented in the following. We follow close to the derivations presented in [23]. Inserting the correlation function introduced in (2.25) into (2.24) yields

$$G(1, 1') = G_0(1, 1') + G_0(1, \bar{2}) v_H(\bar{2}) G(\bar{2}, 1) + i G_0(1, \bar{2}) v_c(\bar{2}, \bar{3}) L(\bar{2}, \bar{3}^+, 1', \bar{3}^{++}). \quad (\text{A.5})$$

Starting from here integrals are denoted using a bar, e.g. $f(\bar{2}) = \int d2 f(2)$. G_0 describes the one-particle Green's function of independent electrons in an external potential, satisfying the equation of motion

$$\left[i \frac{\partial}{\partial t_1} - h(\mathbf{r}_1) \right] G_0(1, 1') = \delta(1, 1'). \quad (\text{A.6})$$

As a consequence of the Martin-Schwinger hierarchy, even the calculation of the one-particle Green's function G_1 requires knowledge of higher-order Green's functions. This makes a direct solution infeasible. A workaround is to express L as a variation of the one-particle Green's function with respect to a fictitious perturbation u , which vanishes at the end of the calculation. This approach leads to a set of first-order differential equations for G , called Schwinger-Dyson equations [23].

The correlation function is then given by

$$L(1, 2, 1', 2') = \left[\frac{\delta G(1, 1')[u]}{\delta u(2, 2')} \right]_{u=0}, \quad (\text{A.7})$$

and the Green's function G_u in the presence of u satisfies

$$\frac{\delta G(2, 1')}{\delta u(3)} = L_u(2, 3, 1', 3^+), \quad (\text{A.8})$$

with a L_u , the two-particle correlation function as a functional of u , and a local fictitious potential $u(3) \equiv u(3, 3^+)$. This allows (A.5) to be written in the presence of u as [23]

$$G_u(1, 1') = G_0(1, 1') + G_0(1, \bar{2}) \left[\{u(\bar{2}) + v_H(\bar{2})\} G_u(\bar{2}, 1) + iv_c(\bar{2}, \bar{3}) \frac{G_u(\bar{2}, 1')}{u(\bar{3}^+)} \right]. \quad (\text{A.9})$$

The inverse Green's function G_u^{-1} follows as

$$G_u^{-1}(1, 1') = G_0^{-1}(1, 1') - \{u(1) + v_H(1)\} \delta(1, 1') - iv_c(1, \bar{3}) \frac{\delta G_u(1, \bar{2})}{u(\bar{3}^+)} G_u^{-1}(\bar{2}, 1'). \quad (\text{A.10})$$

All contributions to the non-interacting propagation appear additively. Therefore, it is convenient to define the exchange-correlation self energy [23]

$$\Sigma_{xc} = iv_c(1, \bar{3}) \left[\frac{\delta G(1, \bar{2})}{\delta u(\bar{3}^+)} \right] G^{-1}(\bar{2}, 1') = -iv_c(1, \bar{3}) G(1, \bar{2}) \left[\frac{\delta G^{-1}(\bar{2}, 1')}{\delta u(\bar{3}^+)} \right] \quad (\text{A.11})$$

where starting here the subscript u is omitted. In fact, (A.9) remains well behaved in the limit of $u \rightarrow 0$, and using the definition of the self energy $\Sigma(1, 2) = v_H(1)\delta(1, 2) + \Sigma_{xc}(1, 2)$, one obtains the Dyson equation for G_1 [80]

$$G(1, 1') = G_0(1, 1') + G_0(1, \bar{2}) \Sigma(\bar{2}, \bar{2}') G(\bar{2}', 1'). \quad (\text{A.12})$$

Analogously, a Dyson-like equation can be derived for the two-particle Green's function or correlation function. Starting from

$$L(1, 2, 1', 2') = -G(1, \bar{3}) \frac{\delta G^{-1}(\bar{3}, \bar{3}') [u]}{\delta u(2', 2)} G(\bar{3}', 1'), \quad (\text{A.13})$$

and using A.10 together with the definition of Σ , one obtains

$$L(1, 2, 1', 2') = G(1, 2') G(2, 1') + G(1, \bar{3}) \frac{\Sigma(\bar{3}, \bar{3}') [u]}{\delta u(2', 2)} G(\bar{3}', 1'). \quad (\text{A.14})$$

Since the exchange-correlation self-energy Σ_{xc} is a functional of the Green's function itself, the derivative with respect to u can be expanded via the chain rule as

$$\frac{\delta \Sigma(\bar{3}, \bar{3}')}{\delta u(2', 2)} = \frac{\delta \Sigma(\bar{3}, \bar{3}')}{\delta G(\bar{4}, \bar{4}')} \frac{\delta G(\bar{4}, \bar{4}')}{\delta u(2', 2)} = \frac{\delta \Sigma(\bar{3}, \bar{3}')}{\delta G(\bar{4}, \bar{4}')} L(\bar{4}, 2, \bar{4}', 2'), \quad (\text{A.15})$$

using the definition of L in (A.7).

With $n(1) = -iG(1, 1^+)$ and hence $v_H(\bar{3}) = -iG(\bar{4}, 4)v_c(\bar{4}, \bar{3})$, one can define the two-particle interaction kernel as [23, 41]

$$\Xi(\bar{3}, \bar{4}, \bar{3}', \bar{4}') = \frac{\delta \Sigma(\bar{3}, \bar{3}')}{\delta G(\bar{4}', \bar{4})} = -i\delta(\bar{3}, \bar{3}') \delta(\bar{4}'^+, \bar{4}) v_c(\bar{4}, \bar{3}^+) + \frac{\delta \Sigma_{xc}(\bar{3}, \bar{3}')}{\delta G(\bar{4}', \bar{4})}. \quad (\text{A.16})$$

Consequently, inserting (A.16) in (A.14) finally yields

$$L(1, 2, 1', 2') = L_0(1, 2, 1', 2') + L_0(1, \bar{3}', 1', \bar{3}') \Xi(\bar{3}, \bar{4}, \bar{3}', \bar{4}') L(\bar{4}', 2, \bar{4}, 2'), \quad (\text{A.17})$$

with

$$L_0(1, 2, 1', 2') = G(1, 2') G(2, 1'). \quad (\text{A.18})$$

A.3 Hedin's equations and GW approximation

In the following we Hedin's equations and their connection to the GW approximation. Up to now, closed equations for the one- and two-particle Green's functions have been obtained by introducing the self-energy Σ and employing a fictitious potential u . In solids, strong screening effects are expected. Therefore, it is convenient to introduce the dynamically screened Coulomb potential W and expand the self-energy Σ in terms of W rather than in terms of the bare Coulomb potential v_c [81, 82]. Using this expansion, Hedin and Lundquist formulated the many-body problem as a self-consistent set of five coupled integral equations, commonly referred to as Hedin's equations:

$$\Sigma_{xc}(1, 2) = iG(1, \bar{4})W(1^+, \bar{3})\Gamma(\bar{4}, 2; \bar{3}) \quad (\text{A.19})$$

$$W(1, 2) = v_c(1, 2) + v_c(1, \bar{3})P(\bar{3}, \bar{4})W(\bar{4}, 2) \quad (\text{A.20})$$

$$P(1, 2) = -iG(1, \bar{3})G(\bar{4}, 1)\Gamma(\bar{3}, \bar{4}; 2) \quad (\text{A.21})$$

$$\Gamma(1, 2; 3) = \delta(1, 2)\delta(1, 3) + \frac{\delta\Sigma_{xc}(1, 2)}{\delta G(\bar{4}, \bar{5})}G(\bar{4}, \bar{6})G(\bar{7}, \bar{5})\Gamma(\bar{6}, \bar{7}; 3) \quad (\text{A.22})$$

$$G(1, 2) = G_0(1, 2) + G_0(1, \bar{3})\Sigma(\bar{3}, \bar{4})G(\bar{4}, 2) \quad (\text{A.23})$$

In these equations, the screened Coulomb interaction is connected to the Coulomb potential v_c via

$$W(1, 2) = \epsilon^{-1}(1, \bar{3})v_c(\bar{3}, 2), \quad (\text{A.24})$$

which also defines the inverse dielectric function ϵ^{-1} . Furthermore, $P(1, 2)$ is the irreducible polarization and $\Gamma(1, 2; 3)$ the vertex function. The full (reducible) polarization χ is related by $\chi = P + Pv_c\chi$ and given by

$$\chi(1, 2) = -i\frac{G(1, 1^+)}{\delta v(2^+, 2)} = -iL(1, 2, 1^+, 2^+). \quad (\text{A.25})$$

Hedin's equations also emphasize the physical importance of the polarization, as P describes the system's response to an additional particle or hole. The polarization arises from the creation of electron-hole pairs, as indicated by the two Green's functions, while the information about the electron-hole interaction, is contained in the vertex function Γ [1].

Hedin's equations are in principal exact, but solving them is a challenging task. Consequently, an iterative approach is a commonly used, typically starting with an approximate self-energy $\Sigma_{xc} = 0$ or an approximate vertex $\Gamma = \delta$. Once the functional form of Hedin's equations is established, they can be evaluated iteratively, starting from an approximate Green's function G , such as Hartree-Fock or Kohn-Sham, as a starting point. The equations (A.19)-(A.23) can then be solved sequentially.

A widely used popular approximation is given by the random phase approximation (RPA) [83–85], which neglects vertex corrections by setting $\Gamma(1, 2; 3) = \delta(1, 2)\delta(1, 3)$. This reduces the polarizability to

$$P(1, 2) \approx P_0(1, 2) = -iG(1, 2^+)G(2, 1^+). \quad (\text{A.26})$$

which corresponds to the independent-particle approximation, where the response function is constructed solely from non-interacting electron-hole pairs. Consequently, the exchange-correlation self-energy becomes

$$\Sigma_{xc}^{GW}(1, 2) \approx iG(1, 2)W(2, 1^+). \quad (\text{A.27})$$

Due to this characteristic expression, $\Sigma = iGW$, this approach is known as the *GW*-Approximation. If, in addition to this approximation, one also just does a one-shot calculation of Hedin's equations, using a fixed Green's Function G_0 , the resulting approach is referred to as G_0W_0 -Approximation.

A.4 RIXS in the IPA

We present the detailed derivation of the RIXS cross section within the independent-particle approximation following close to the approach presented in [3]. From

$$\left. \frac{d^2\sigma}{d\Omega_2 d\omega_2} \right|_{IP} = \alpha^4 \left(\frac{\omega_2}{\omega_1} \right) \sum_{c'v\mathbf{k}'} \left| \sum_{c\mu\mathbf{k}} \frac{\langle c'v\mathbf{k}' | \hat{T}^\dagger(\mathbf{e}_2) | c\mu\mathbf{k} \rangle \langle c\mu\mathbf{k} | \hat{T}(\mathbf{e}_1) | 0 \rangle}{\omega_1 - (\epsilon_{c\mathbf{k}} - \epsilon_{\mu\mathbf{k}}) + i\eta} \right|^2 \delta(\omega - (\epsilon_{c'\mathbf{k}'} - \epsilon_{v\mathbf{k}})), \quad (\text{A.28})$$

with the transition operator expressed as

$$\hat{T}(\mathbf{e}) = \mathbf{e} \sum_j \mathbf{p}_j = \sum_{mn} \sum_{\mathbf{k}} [\mathbf{e}_1 \cdot \mathbf{P}_{m\mathbf{n}\mathbf{k}}] \hat{c}_{m\mathbf{k}}^\dagger \hat{c}_{n\mathbf{k}}, \quad (\text{A.29})$$

follows

$$\begin{aligned} \left. \frac{d^2\sigma}{d\Omega_2 d\omega_2} \right|_{IP} &= \alpha^4 \left(\frac{\omega_2}{\omega_1} \right) \sum_{c'v\mathbf{k}'} \left| \sum_{c\mu\mathbf{k}} \sum_{m\mathbf{n}\mathbf{k}''} \sum_{p\mathbf{q}\mathbf{k}'''} [\mathbf{e}_2^* \cdot \mathbf{P}_{m\mathbf{n}\mathbf{k}''}] \times \right. \\ &\quad \times \left. \frac{\langle c'v\mathbf{k}' | \hat{c}_{m\mathbf{k}''}^\dagger \hat{c}_{n\mathbf{k}''} | c\mu\mathbf{k} \rangle \langle c\mu\mathbf{k} | \hat{c}_{p\mathbf{k}'''}^\dagger \hat{c}_{q\mathbf{k}'''} | 0 \rangle}{\omega_1 - (\epsilon_{c\mathbf{k}} - \epsilon_{\mu\mathbf{k}}) + i\eta} [\mathbf{P}_{p\mathbf{q}\mathbf{k}'''} \cdot \mathbf{e}_1] \right|^2 \delta(\omega - (\epsilon_{c'\mathbf{k}'} - \epsilon_{v\mathbf{k}})). \end{aligned} \quad (\text{A.30})$$

The summation over p and q is not restricted to either core, valence or conduction states. In fact, restrictions arise from matrix elements involving creation and annihilation operators. For the second term states

$$\langle c\mu\mathbf{k} | \hat{c}_{p\mathbf{k}'''}^\dagger \hat{c}_{q\mathbf{k}'''} | 0 \rangle = \langle 0 | \hat{c}_{\mu\mathbf{k}}^\dagger \hat{c}_{c\mathbf{k}} \hat{c}_{p\mathbf{k}'''}^\dagger \hat{c}_{q\mathbf{k}'''} | 0 \rangle = \delta_{\mu q} \delta_{cp} \delta_{\mathbf{k}\mathbf{k}''}. \quad (\text{A.31})$$

For the first term Wick's theorem [47, 86] has to be employed, yielding

$$\begin{aligned} \langle c'v\mathbf{k}' | \hat{c}_{m\mathbf{k}''}^\dagger \hat{c}_{n\mathbf{k}''} | c\mu\mathbf{k} \rangle &= \langle 0 | \left[\hat{c}_{v\mathbf{k}'}^\dagger \hat{c}_{n\mathbf{k}''} \right] \left[\hat{c}_{m\mathbf{k}''}^\dagger \hat{c}_{n\mathbf{k}''} \right] \left[\hat{c}_{c'\mathbf{k}'}^\dagger \hat{c}_{\mu\mathbf{k}} \right] | 0 \rangle \\ &= \delta_{v\mu} \delta_{c'n} \delta_{cm} \delta_{\mathbf{k}\mathbf{k}''} \delta_{\mathbf{k}\mathbf{k}''} + \delta_{cc'} \delta_{mn} \delta_{v\mu} \delta_{\mathbf{k}\mathbf{k}'} \delta_{\mathbf{k}\mathbf{k}''} - \delta_{cc'} \delta_{\mu m} \delta_{vn} \delta_{\mathbf{k}\mathbf{k}'} \delta_{\mathbf{k}\mathbf{k}''}. \end{aligned} \quad (\text{A.32})$$

Inserting this result into (A.30) yields the cross section as a sum of three terms and additional cross terms because of the square. Neglecting interference terms, we obtain

$$\begin{aligned} \left. \frac{d^2\sigma}{d\Omega_2 d\omega_2} \right|_{IP} &= \alpha^4 \left(\frac{\omega_2}{\omega_1} \right) \left\{ \sum_{c'\mu\mathbf{k}} \left| \sum_c \frac{[\mathbf{e}_2^* \cdot \mathbf{P}_{c'\mathbf{k}}] [\mathbf{P}_{c\mu\mathbf{k}} \cdot \mathbf{e}_1]}{\omega_1 - (\epsilon_{c\mathbf{k}} - \epsilon_{\mu\mathbf{k}}) + i\eta} \right|^2 \delta(\omega - (\epsilon_{c'\mathbf{k}'} - \epsilon_{\mu\mathbf{k}})) \quad (\text{i}) \right. \\ &\quad + \sum_{c\mu\mathbf{k}} \left| \sum_m \frac{[\mathbf{e}_2^* \cdot \mathbf{P}_{m\mathbf{k}}] [\mathbf{P}_{c\mu\mathbf{k}} \cdot \mathbf{e}_1]}{\omega_1 - (\epsilon_{c\mathbf{k}} - \epsilon_{\mu\mathbf{k}}) + i\eta} \right|^2 \delta(\omega - (\epsilon_{c\mathbf{k}} - \epsilon_{\mu\mathbf{k}})) \quad (\text{ii}) \\ &\quad \left. + \sum_{c\nu\mathbf{k}} \left| \sum_\mu \frac{[\mathbf{e}_2^* \cdot \mathbf{P}_{\mu\nu\mathbf{k}}] [\mathbf{P}_{c\mu\mathbf{k}} \cdot \mathbf{e}_1]}{\omega_1 - (\epsilon_{c\mathbf{k}} - \epsilon_{\mu\mathbf{k}}) + i\eta} \right|^2 \delta(\omega - (\epsilon_{c\mathbf{k}} - \epsilon_{\nu\mathbf{k}})) \right\}. \quad (\text{iii}) \end{aligned} \quad (\text{A.33})$$

Let us analyze the three single terms in more detail:

The first term (i) does not correspond to the RIXS process. Its excitation energy poles lie at $\omega_1 = \epsilon_{c\mathbf{k}} - \epsilon_{\mu\mathbf{k}}$, describing the excitation of a core electron into a conduction state.

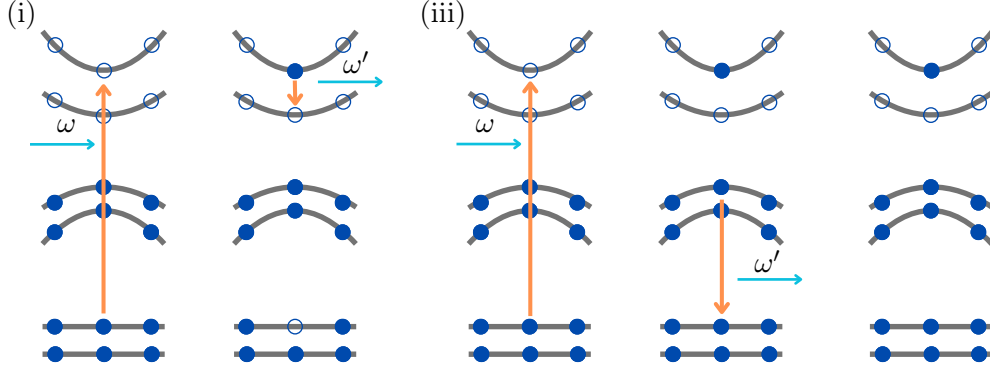


Figure 18: Schema of the processes contributing to the RIXS cross section in (A.33) within the independent particle approximation. Filled and open circles represent occupied and unoccupied states. Orange lines represent transitions and light blue lines x-ray absorption and transmission

Accordingly, the corresponding emission energy poles occur at $\omega_2 = \epsilon_{c\mathbf{k}} - \epsilon_{c'\mathbf{k}}$, which describes the transition of an electron from one conduction state to another. Consequently, the final state described by this term consists of a hole in a core state and an excited electron in a conduction state, which isn't the aspired RIXS finale state. The transition is schematically shown in Figure 18.

The second term (ii) can also be neglected, as it does not describe a resonant scattering process. Poles occur at $\omega_1 = \epsilon_{c\mathbf{k}} - \epsilon_{\mu\mathbf{k}}$ and $\omega_2 = 0$, while the emission corresponds to the $m\mathbf{k} \rightarrow m\mathbf{k}$ transition. However, since m runs over all valence and conduction states and the occupation factor $f_{m\mathbf{k}}$ needs to be included, one obtains $\mathbf{P}_{mm\mathbf{k}} = f_{m\mathbf{k}}(1 - f_{m\mathbf{k}})\langle m\mathbf{k}|\hat{\mathbf{p}}|m\mathbf{k}\rangle$. Both, for conduction states ($f_{m\mathbf{k}} = 0$) and valence states ($f_{m\mathbf{k}} = 1$) this states $\mathbf{P}_{mm\mathbf{k}} = 0$ for all m .

Consequently, the remaining term (iii) corresponds to the desired RIXS process. The term has poles at the excitation energies $\omega_1 = \epsilon_{c\mathbf{k}} - \epsilon_{\mu\mathbf{k}}$ and the emission energies $\omega_2 = \epsilon_{v\mathbf{k}} - \epsilon_{\mu\mathbf{k}}$. This exactly corresponds to the RIXS process, describing first an excitation $\mu\mathbf{k} \rightarrow c\mathbf{k}$ from a core state to a conduction state and subsequently the de-excitation $v\mathbf{k} \rightarrow \mu\mathbf{k}$ from a valence state into the core hole. The final state then consists of a valence hole and an excited electron in the conduction state.

Following this discussion, the corresponding matrix element simplifies to

$$\langle cv\mathbf{k}|\hat{c}_{m\mathbf{k}'}^\dagger\hat{c}_{n\mathbf{k}''}|c'\mu\mathbf{k}'\rangle = -\delta_{cc'}\delta_{\mu m}\delta_{vn}\delta_{\mathbf{k}\mathbf{k}'}\delta_{\mathbf{k}\mathbf{k}''}, \quad (\text{A.34})$$

and the RIXS cross section becomes

$$\left.\frac{d^2\sigma}{d\Omega_2 d\omega_2}\right|_{IP} = \alpha^4 \left(\frac{\omega_2}{\omega_1}\right) \sum_{cv\mu\mathbf{k}} \left| \frac{[\mathbf{e}_2^* \cdot \mathbf{P}_{\mu v\mathbf{k}}][\mathbf{P}_{c\mu\mathbf{k}} \cdot \mathbf{e}_1]}{\omega_1 - (\epsilon_{c\mathbf{k}} - \epsilon_{\mu\mathbf{k}}) + i\eta} \right|^2 \delta(\omega - (\epsilon_{c\mathbf{k}} - \epsilon_{v\mathbf{k}})). \quad (\text{A.35})$$

A.5 RIXS in many-body perturbation theory

We present the expansion of the RIXS DDCCS within the MBPT framework. We follow close to the derivations presented in [3]. An intermediate many-body state can be defined as [16, 87]

$$|Y(\omega_1)\rangle = \sum_n \frac{|n\rangle\langle n|}{\omega_1 - E_n} \hat{T}(\mathbf{e}_1)|0\rangle. \quad (\text{A.36})$$

Inserting this into (2.44) yields

$$\frac{d^2\sigma}{d\Omega_2 d\omega_2} = \alpha^4 \left(\frac{\omega_2}{\omega_1} \right) \sum_f \langle Y(\omega_1) | \hat{T}(\mathbf{e}_2) | f \rangle \langle f | \hat{T}^\dagger(\mathbf{e}_2) | Y(\omega_2) \rangle \delta(\omega - E_f), \quad (\text{A.37})$$

such that all information about possible excitation processes are contained within $Y(\omega)$. Expressing the δ -function according to (2.49) and introducing a lifetime broadening η yields

$$\frac{d^2\sigma}{d\Omega_2 d\omega_2} = \alpha^4 \left(\frac{\omega_2}{\omega_1} \right) \text{Im} \sum_f \frac{\langle Y(\omega_1) | \hat{T}(\mathbf{e}_2) | f \rangle \langle f | \hat{T}^\dagger(\mathbf{e}_2) | Y(\omega_2) \rangle}{\omega - E_f + i\eta}. \quad (\text{A.38})$$

Within the Tamm-Dancoff approximation, we assume that both the intermediate and final many-body states can be expressed as linear combinations of singlet excitations. Thus, they only consist of one electron-hole pair per state and they can be represented in terms of creation and annihilation operators. Unity can be approximated by

$$\mathbb{1} \approx \sum_{i\mathbf{k}} \sum_{j\mathbf{k}'} \hat{c}_{j\mathbf{k}'}^\dagger \hat{c}_{i\mathbf{k}} |0\rangle \langle 0| \hat{c}_{i\mathbf{k}}^\dagger \hat{c}_{j\mathbf{k}'}. \quad (\text{A.39})$$

It should be noted, that applying this approximation, the considerations is limited onto direct RIXS processes. Indirect RIXS can not be described anymore, since this requires the presence of two electron-hole pairs. Inserting (A.39) into (A.38) twice and using the definition of the transition operator $\hat{T}(\mathbf{e})$ yields

$$\begin{aligned} \frac{d^2\sigma}{d\Omega_2 d\omega_2} &= \alpha^4 \left(\frac{\omega_2}{\omega_1} \right) \text{Im} \sum_f \sum_{ij\mathbf{k}} \sum_{l\mathbf{k}''} \sum_{m\mathbf{k}''' } \sum_{n\mathbf{k}^{IV}} \sum_{o\mathbf{k}^V} \sum_{pq\mathbf{k}^{VI}} [\mathbf{e}_2^* \cdot \mathbf{P}_{ij\mathbf{k}}] \times \\ &\quad \times \langle Y(\omega_1) | \hat{c}_{j\mathbf{k}}^\dagger \hat{c}_{i\mathbf{k}} \hat{c}_{m\mathbf{k}'''}^\dagger \hat{c}_{l\mathbf{k}''}^\dagger |0\rangle \frac{\langle 0 | \hat{c}_{l\mathbf{k}''}^\dagger \hat{c}_{m\mathbf{k}'''} | f \rangle \langle f | \hat{c}_{o\mathbf{k}^V}^\dagger \hat{c}_{n\mathbf{k}^{IV}} |0\rangle}{\omega - E_f + i\eta} \times \\ &\quad \times \langle 0 | \hat{c}_{n\mathbf{k}^{IV}}^\dagger \hat{c}_{o\mathbf{k}^V} \hat{c}_{p\mathbf{k}^{VI}}^\dagger \hat{c}_{q\mathbf{k}^{VI}} | Y(\omega_1) \rangle [\mathbf{e}_2^* \cdot \mathbf{P}_{pq\mathbf{k}^{VI}}] \quad (\text{A.40}) \\ &= \alpha^4 \left(\frac{\omega_2}{\omega_1} \right) \text{Im} \sum_{ij\mathbf{k}} \sum_{l\mathbf{k}''} \sum_{m\mathbf{k}'''} \sum_{n\mathbf{k}^{IV}} \sum_{o\mathbf{k}^V} \sum_{pq\mathbf{k}^{VI}} [\mathbf{e}_2^* \cdot \mathbf{P}_{ij\mathbf{k}}] \times \\ &\quad \times \langle Y(\omega_1) | \hat{c}_{j\mathbf{k}}^\dagger \hat{c}_{i\mathbf{k}} \hat{c}_{m\mathbf{k}'''}^\dagger \hat{c}_{l\mathbf{k}''}^\dagger |0\rangle \chi_{m\mathbf{k}''', l\mathbf{k}'', n\mathbf{k}^{IV}, o\mathbf{k}^V}(\omega) \times \\ &\quad \times \langle 0 | \hat{c}_{n\mathbf{k}^{IV}}^\dagger \hat{c}_{o\mathbf{k}^V} \hat{c}_{p\mathbf{k}^{VI}}^\dagger \hat{c}_{q\mathbf{k}^{VI}} | Y(\omega_1) \rangle [\mathbf{e}_2^* \cdot \mathbf{P}_{pq\mathbf{k}^{VI}}]. \end{aligned}$$

In the second step, the Lehmann representation of the polarizability χ was used, such that the summation over the final states is now only implicitly included in the polarizability. Furthermore, within the IPA, summations over indices of creating and annihilation operators directly acting on the ground state are limited to conduction and valence states. Thus, we obtain

$$\begin{aligned} \frac{d^2\sigma}{d\Omega_2 d\omega_2} &= \alpha^4 \left(\frac{\omega_2}{\omega_1} \right) \text{Im} \sum_{ij\mathbf{k}} \sum_{c\mathbf{k}_c} \sum_{v\mathbf{k}_v} \sum_{c'\mathbf{k}'_c} \sum_{v\mathbf{k}'_v} \sum_{lm\mathbf{k}'} [\mathbf{e}_2^* \cdot \mathbf{P}_{ij\mathbf{k}}] \langle Y(\omega_1) | \hat{c}_{j\mathbf{k}}^\dagger \hat{c}_{i\mathbf{k}} \hat{c}_{c\mathbf{k}_c}^\dagger \hat{c}_{v\mathbf{k}_v} |0\rangle \times \\ &\quad \times \chi_{c\mathbf{k}_c, v\mathbf{k}_v, c'\mathbf{k}'_c, v\mathbf{k}'_v}(\omega) \langle 0 | \hat{c}_{v\mathbf{k}'_v}^\dagger \hat{c}_{c'\mathbf{k}'_c} \hat{c}_{l\mathbf{k}'}^\dagger \hat{c}_{m\mathbf{k}'} | Y(\omega_1) \rangle [\mathbf{e}_2^* \cdot \mathbf{P}_{lm\mathbf{k}'}]. \quad (\text{A.41}) \end{aligned}$$

In contrast, the summations over $(ij\mathbf{k})$ and $(lm\mathbf{k}')$ are not restricted, as they do not act on a ground state, rather on the many-body state $|Y(\omega_1)\rangle$. Before evaluating the expectation values containing $Y(\omega_1)$ let us look at the state itself and use the arguments analogously to the discussion of (A.33). The intermediate state should contain a core hole and therefore the expression of the unity in (A.39) is adapted to a conduction electron and core hole. The

intermediate many-body state is then, again using the definition of the transition operator $\hat{T}(\mathbf{e})$, described by

$$\begin{aligned}
|Y(\omega_1)\rangle &= \sum_n \sum_{c\mu\mathbf{k}} \sum_{c'\mu'\mathbf{k}'} |\hat{c}_{c\mathbf{k}}^\dagger \hat{c}_{\mu\mathbf{k}}|0\rangle \frac{\langle 0|\hat{c}_{\mu\mathbf{k}}^\dagger \hat{c}_{c\mathbf{k}}|n\rangle \langle n|\hat{c}_{c'\mathbf{k}'}^\dagger \hat{c}_{\mu'\mathbf{k}'}|0\rangle}{\omega_1 - E_n} [\mathbf{e}_1 \cdot \mathbf{P}_{c'\mu'\mathbf{k}'}] \\
&= \sum_{c\mu\mathbf{k}} \sum_{c'\mu'\mathbf{k}'} |\hat{c}_{c\mathbf{k}}^\dagger \hat{c}_{\mu\mathbf{k}}|0\rangle \chi_{c\mu\mathbf{k},c'\mu'\mathbf{k}'}(\omega_1) [\mathbf{e}_1 \cdot \mathbf{P}_{c'\mu'\mathbf{k}'}].
\end{aligned} \tag{A.42}$$

The corresponding expectation value of the intermediate state then yields

$$\begin{aligned}
\langle Y(\omega_1)|\hat{c}_{j\mathbf{k}}^\dagger \hat{c}_{i\mathbf{k}} \hat{c}_{c\mathbf{k}_c}^\dagger \hat{c}_{v\mathbf{k}_v}|0\rangle &= \sum_{c\mu\mathbf{k}} \sum_{c'\mu'\mathbf{k}'} \chi_{c\mu\mathbf{k},c'\mu'\mathbf{k}'}(\omega_1) [\mathbf{e}_1 \cdot \mathbf{P}_{c'\mu'\mathbf{k}'}]^* \times \\
&\quad \times \langle 0|\hat{c}_{\mu\mathbf{k}}^\dagger \hat{c}_{\mu\mathbf{k}} \hat{c}_{j\mathbf{k}''}^\dagger \hat{c}_{i\mathbf{k}''} \hat{c}_{c''\mu''\mathbf{k}''}^\dagger \hat{c}_{v''\mu''\mathbf{k}''}|0\rangle \\
&= - \sum_{c\mu\mathbf{k}} \sum_{c'\mu'\mathbf{k}'} \chi_{c\mu\mathbf{k},c'\mu'\mathbf{k}'}(\omega_1) [\mathbf{e}_1 \cdot \mathbf{P}_{c'\mu'\mathbf{k}'}]^* \delta_{cc''} \delta_{v''j} \delta_{\mu i} \delta_{\mathbf{k}\mathbf{k}''} \delta_{\mathbf{k}\mathbf{k}''},
\end{aligned} \tag{A.43}$$

using (A.34). This finally concludes the RIXS cross section to

$$\begin{aligned}
\frac{d^2\sigma}{d\Omega_2 d\omega_2} &= \alpha^4 \left(\frac{\omega_2}{\omega_1}\right) \text{Im} \sum_{cc''c'''} \sum_{\mu\mu'\mu''\mu'''} \sum_{vv'} \sum_{\mathbf{k}\mathbf{k}'\mathbf{k}''\mathbf{k}'''} \left[[\mathbf{e}_2^* \cdot \mathbf{P}_{\mu v\mathbf{k}}] \chi_{c\mu\mathbf{k},c'\mu'\mathbf{k}'}(\omega_1) [\mathbf{e}_1 \cdot \mathbf{P}_{c'\mu'\mathbf{k}'}] \right]^* \\
&\quad \times \chi_{c''v\mathbf{k},c'''\mu''\mathbf{k}''}(\omega) \left[[\mathbf{e}_2^* \cdot \mathbf{P}_{\mu'' v''\mathbf{k}''}] \chi_{c''\mu''\mathbf{k}'',c'''\mu'''\mathbf{k}'''}(\omega_1) [\mathbf{e}_1 \cdot \mathbf{P}_{c'''\mu'''\mathbf{k}'''}] \right].
\end{aligned} \tag{A.44}$$

References

- [1] G. Onida, L. Reining, and A. Rubio, “Electronic excitations: density-functional versus many-body green’s-function approaches”, *Rev. Mod. Phys.* **74**, 601–659 (2002).
- [2] M. Rohlfing and S. G. Louie, “Electron-hole excitations and optical spectra from first principles”, *Phys. Rev. B* **62**, 4927–4944 (2000).
- [3] C. W. Vorwerk, “Theoretical spectroscopy of Ga_2O_3 ”, PhD thesis (Humboldt-Universität zu Berlin, Mathematisch-Naturwissenschaftliche Fakultät, 2021).
- [4] C. Vorwerk, F. Sottile, and C. Draxl, “Excitation pathways in resonant inelastic x-ray scattering of solids”, *Physical Review Research* **2**, 10.1103/physrevresearch.2.042003 (2020).
- [5] C. Vorwerk, F. Sottile, and C. Draxl, “All-electron many-body approach to resonant inelastic x-ray scattering”, *Physical Chemistry Chemical Physics* **24**, 17439–17448 (2022).
- [6] L. J. P. Ament, M. van Veenendaal, T. P. Devereaux, J. P. Hill, and J. van den Brink, “Resonant inelastic x-ray scattering studies of elementary excitations”, *Rev. Mod. Phys.* **83**, 705–767 (2011).
- [7] Y. Chen, Y. Wang, C. Jia, B. Moritz, A. M. Shvaika, J. K. Freericks, and T. P. Devereaux, “Theory for time-resolved resonant inelastic x-ray scattering”, *Phys. Rev. B* **99**, 104306 (2019).
- [8] F. Bonaccorso, Z. Sun, T. Hasan, and A. C. Ferrari, “Graphene photonics and optoelectronics”, *Nature photonics* **4**, 611–622 (2010).
- [9] M. S. Dresselhaus and G. Dresselhaus, “Intercalation compounds of graphite”, *Advances in physics* **51**, 1–186 (2002).
- [10] P. E. Trevisanutto, M. Holzmann, M. Côté, and V. Olevano, “Ab initio high-energy excitonic effects in graphite and graphene”, *Phys. Rev. B* **81**, 121405 (2010).
- [11] A. G. Marinopoulos, L. Reining, A. Rubio, and V. Olevano, “Ab initio study of the optical absorption and wave-vector-dependent dielectric response of graphite”, *Phys. Rev. B* **69**, 245419 (2004).
- [12] E. L. Shirley, “Ab initio inclusion of electron-hole attraction: application to x-ray absorption and resonant inelastic x-ray scattering”, *Phys. Rev. Lett.* **80**, 794–797 (1998).
- [13] M. Unzog, A. Tal, and G. Kresse, “X-ray absorption using the projector augmented-wave method and the bethe-salpeter equation”, *Phys. Rev. B* **106**, 155133 (2022).
- [14] J. A. Carlisle, E. L. Shirley, E. A. Hudson, L. J. Terminello, T. A. Callcott, J. J. Jia, D. L. Ederer, R. C. C. Perera, and F. J. Himpsel, “Probing the graphite band structure with resonant soft-x-ray fluorescence”, *Phys. Rev. Lett.* **74**, 1234–1237 (1995).
- [15] J. A. Carlisle, E. L. Shirley, L. J. Terminello, J. J. Jia, T. A. Callcott, D. L. Ederer, R. C. C. Perera, and F. J. Himpsel, “Band-structure and core-hole effects in resonant inelastic soft-x-ray scattering: experiment and theory”, *Phys. Rev. B* **59**, 7433–7445 (1999).
- [16] E. Shirley, “Core and final-state excitonic effects and resonant inelastic x-ray scattering in s-p bonded solids”, *Journal of Physics and Chemistry of Solids* **61**, 445–447 (2000).

- [17] E. L. Shirley, “Theory and simulation of resonant inelastic x-ray scattering in s–p bonded systems: graphite, hexagonal boron nitride, diamond, and cubic boron nitride”, *Journal of Electron Spectroscopy and Related Phenomena* **110-111**, Soft X Ray Emission Spectroscopy, 305–321 (2000).
- [18] L. Zhang, N. Schwertfager, T. Cheiwchanchamnangij, X. Lin, P.-A. Glans-Suzuki, L. F. J. Piper, S. Limpijumnong, Y. Luo, J. F. Zhu, W. R. L. Lambrecht, and J.-H. Guo, “Electronic band structure of graphene from resonant soft x-ray spectroscopy: the role of core-hole effects”, *Phys. Rev. B* **86**, 245430 (2012).
- [19] C. D. Dashwood, A. Geondzhian, J. G. Vale, A. C. Pakpour-Tabrizi, C. A. Howard, Q. Faure, L. S. I. Veiga, D. Meyers, S. G. Chiuzašan, A. Nicolaou, N. Jaouen, R. B. Jackman, A. Nag, M. Garcia-Fernandez, K.-J. Zhou, A. C. Walters, K. Gilmore, D. F. McMorrow, and M. P. M. Dean, “Probing electron-phonon interactions away from the fermi level with resonant inelastic x-ray scattering”, *Phys. Rev. X* **11**, 041052 (2021).
- [20] X. Gao, “Development of polarization analysis of resonant inelastic x-ray scattering”, PhD thesis (Western Michigan University, 2013).
- [21] A. Yasui, Y. Kayanuma, S. Tanaka, and Y. Harada, “Dynamical changeover of core exciton state of graphite and resonant x-ray emission spectrum: from shallow to deep level with symmetry breaking”, *Phys. Rev. B* **74**, 205404 (2006).
- [22] M. Malvestuto, B. Volpato, E. Babici, R. Bhardwaj, A. Caretta, S. Laterza, F. Parmigiani, M. Manfreda, A. Simoncig, M. Zangrando, A. Demidovich, P. Susnjar, E. M. Allaria, A. D. Brynes, D. Garzella, L. Giannessi, P. Rebernik, F. Sottocorona, and D. Novko, *Ultrafast dynamics of vibronically dressed core-excitons in graphite: a femtosecond rixs perspective*, 2025.
- [23] R. M. Martin, L. Reining, and D. Ceperley, *Interacting electrons: theory and computational approaches* (Cambridge University Press, 2016).
- [24] M. Born and R. Oppenheimer, “Zur quantentheorie der molekeln”, *Annalen der Physik* **389**, 457–484 (1927).
- [25] P. Hohenberg and W. Kohn, “Inhomogeneous electron gas”, *Phys. Rev.* **136**, B864–B871 (1964).
- [26] R. M. Martin, *Electronic structure: basic theory and practical methods* (Cambridge University Press, 2004).
- [27] W. Kohn and L. J. Sham, “Self-consistent equations including exchange and correlation effects”, *Phys. Rev.* **140**, A1133–A1138 (1965).
- [28] J. P. Perdew and K. Schmidt, “Jacob’s ladder of density functional approximations for the exchange-correlation energy”, *AIP Conference Proceedings* **577**, 1–20 (2001).
- [29] J. P. Perdew, K. Burke, and M. Ernzerhof, “Generalized gradient approximation made simple”, *Phys. Rev. Lett.* **77**, 3865–3868 (1996).
- [30] J. P. Perdew, A. Ruzsinszky, G. I. Csonka, O. A. Vydrov, G. E. Scuseria, L. A. Constantin, X. Zhou, and K. Burke, “Restoring the density-gradient expansion for exchange in solids and surfaces”, *Phys. Rev. Lett.* **100**, 136406 (2008).
- [31] G.-X. Zhang, A. M. Reilly, A. Tkatchenko, and M. Scheffler, “Performance of various density-functional approximations for cohesive properties of 64 bulk solids”, *eng, New journal of physics* **20**, 63020– (2018).
- [32] M. S. Hybertsen and S. G. Louie, “Electron correlation in semiconductors and insulators: band gaps and quasiparticle energies”, *Phys. Rev. B* **34**, 5390–5413 (1986).

-
- [33] J. P. Perdew, S. Kurth, A. š. Zupan, and P. Blaha, “Accurate density functional with correct formal properties: a step beyond the generalized gradient approximation”, *Phys. Rev. Lett.* **82**, 2544–2547 (1999).
- [34] J. Paier, M. Marsman, K. Hummer, G. Kresse, I. C. Gerber, and J. G. Ángyán, “Screened hybrid density functionals applied to solids”, *The Journal of Chemical Physics* **124**, 154709 (2006).
- [35] M. Marques and E. Gross, “Time-dependent density functional theory”, *Annual Review of Physical Chemistry* **55**, 427–455 (2004).
- [36] E. Runge and E. K. U. Gross, “Density-functional theory for time-dependent systems”, *Phys. Rev. Lett.* **52**, 997–1000 (1984).
- [37] M. Marques and E. Gross, “Time-dependent density functional theory”, *Annual Review of Physical Chemistry* **55**, 427–455 (2004).
- [38] N. T. Maitra, “Perspective: fundamental aspects of time-dependent density functional theory”, *The Journal of Chemical Physics* **144**, 220901 (2016).
- [39] R. Rodrigues Pela and C. Draxl, “All-electron full-potential implementation of real-time tddft in exciting”, *Electronic Structure* **3**, 037001 (2021).
- [40] L. Hedin and S. Lundqvist, “Effects of electron-electron and electron-phonon interactions on the one-electron states of solids”, in *Solid state physics*, edited by F. Seitz, D. Turnbull, and H. Ehrenreich (Academic Press, 1969).
- [41] G. Strinati, “Application of the Green’s functions method to the study of the optical properties of semiconductors”, *Nuovo Cimento Rivista Serie* **11**, 1–86 (1988).
- [42] G. Baym and L. P. Kadanoff, “Conservation laws and correlation functions”, *Phys. Rev.* **124**, 287–299 (1961).
- [43] P. C. Martin and J. Schwinger, “Theory of many-particle systems. i”, *Phys. Rev.* **115**, 1342–1373 (1959).
- [44] E. E. Salpeter and H. A. Bethe, “A relativistic equation for bound-state problems”, *Phys. Rev.* **84**, 1232–1242 (1951).
- [45] P. Puschnig, “Excitonic effects in organic semi-conductors: an ab-initio study within the lapw method”, PhD thesis (University of Graz, 2002).
- [46] S. Sagmeister, “Excitonic effects in solids : time-dependent density functional theory versus the bethe-salpeter equation”, PhD thesis (University of Graz, 2009).
- [47] A. L. Fetter and J. D. Walecka, *Quantum theory of many-particle systems* (McGraw-Hill, Boston, 1971).
- [48] S. L. Adler, “Quantum theory of the dielectric constant in real solids”, *Phys. Rev.* **126**, 413–420 (1962).
- [49] N. Wiser, “Dielectric constant with local field effects included”, *Phys. Rev.* **129**, 62–69 (1963).
- [50] W. Schülke, *Electron dynamics by inelastic x-ray scattering winfried schülke*, Oxford series on synchrotron radiation ; 7 (Oxford University Press, Oxford ; New York, 2007).
- [51] H. A. Kramers and W. Heisenberg, “Über die Streuung von Strahlung durch Atome”, *Zeitschrift fur Physik* **31**, 681–708 (1925).
- [52] P. A. M. Dirac and R. H. Fowler, “The quantum theory of dispersion”, *Proceedings of the Royal Society of London. Series A, Containing Papers of a Mathematical and Physical Character* **114**, 710–728 (1927).

- [53] M. van Veenendaal, X. Liu, M. H. Carpenter, and S. P. Cramer, “Observation of dd excitations in nio and NiCl_2 using K -edge resonant inelastic x-ray scattering”, *Phys. Rev. B* **83**, 045101 (2011).
- [54] A. Gulans, S. Kontur, C. Meisenbichler, D. Nabok, P. Pavone, S. Rigamonti, S. Sagmeister, U. Werner, and C. Draxl, “Exciting: a full-potential all-electron package implementing density-functional theory and many-body perturbation theory”, *Journal of Physics: Condensed Matter* **26**, 363202 (2014).
- [55] A. Gulans, A. Kozhevnikov, and C. Draxl, “Microhartree precision in density functional theory calculations”, *Phys. Rev. B* **97**, 161105 (2018).
- [56] C. Vorwerk, B. Aurich, C. Cocchi, and C. Draxl, “Bethe-salpeter equation for absorption and scattering spectroscopy: implementation in the exciting code”, *Electronic Structure* **1**, 10.1088/2516-1075/ab3123 (2019).
- [57] P. Puschnig and C. Ambrosch-Draxl, “Optical absorption spectra of semiconductors and insulators including electron-hole correlations: an ab initio study within the lapw method”, *Phys. Rev. B* **66**, 165105 (2002).
- [58] C. Vorwerk, C. Cocchi, and C. Draxl, “Addressing electron-hole correlation in core excitations of solids: an all-electron many-body approach from first principles”, *Phys. Rev. B* **95**, 155121 (2017).
- [59] R. Rodrigues Pela and C. Draxl, “All-electron full-potential implementation of real-time tddft in exciting”, *Electronic Structure* **3**, 037001 (2021).
- [60] S. Sagmeister and C. Ambrosch-Draxl, “Time-dependent density functional theory versus bethe–salpeter equation: an all-electron study”, *Phys. Chem. Chem. Phys.* **11**, 4451–4457 (2009).
- [61] R. R. Pela and C. Draxl, “Ehrenfest dynamics implemented in the all-electron package exciting”, *Electronic Structure* **4**, 037001 (2022).
- [62] R. R. Pela and C. Draxl, “Speeding up all-electron real-time tddft demonstrated by the exciting package”, *Computer Physics Communications* **304**, 109292 (2024).
- [63] C. Vorwerk, *BRIXS*, <https://github.com/exciting/BRIXS/>, 2021.
- [64] C. Vorwerk, *pyBRIXS*, <https://github.com/exciting/pyBRIXS/>, 2021.
- [65] M. Inagaki, “Chapter 2.1 - advanced carbon materials”, in *Handbook of advanced ceramics (second edition)*, edited by S. Somiya, Second Edition (Academic Press, Oxford, 2013), pages 25–60.
- [66] Y. Harada, T. Tokushima, Y. Takata, T. Takeuchi, Y. Kitajima, S. Tanaka, Y. Kayanuma, and S. Shin, “Dynamical symmetry breaking under core excitation in graphite: polarization correlation in soft x-ray recombination emission”, *Phys. Rev. Lett.* **93**, 017401 (2004).
- [67] C. Nicolas and C. Miron, “Lifetime broadening of core-excited and-ionized states”, *Journal of Electron Spectroscopy and Related Phenomena* **185**, 267–272 (2012).
- [68] A. Tkatchenko and M. Scheffler, “Accurate molecular van der waals interactions from ground-state electron density and free-atom reference data”, *Phys. Rev. Lett.* **102**, 073005 (2009).
- [69] N. Ooi, A. Rairkar, and J. B. Adams, “Density functional study of graphite bulk and surface properties”, *Carbon* **44**, 231–242 (2006).
- [70] R. C. Tatar and S. Rabii, “Electronic properties of graphite: a unified theoretical study”, *Phys. Rev. B* **25**, 4126–4141 (1982).

-
- [71] J.-C. Charlier, X. Gonze, and J.-P. Michenaud, “First-principles study of the electronic properties of graphite”, *Phys. Rev. B* **43**, 4579–4589 (1991).
- [72] F. Bassani and G. P. Parravicini, “Band structure and optical properties of graphite and of the layer compounds GaS and GaSe”, *Nuovo Cimento B Serie* **50**, 95–128 (1967).
- [73] E. A. Taft and H. R. Philipp, “Optical properties of graphite”, *Phys. Rev.* **138**, A197–A202 (1965).
- [74] E. Tosatti and F. Bassani, “Optical constants of graphite”, *Nuovo Cimento B Serie* **65**, 161–173 (1970).
- [75] K. Zeppenfeld, “Anisotropie der plasmaschwingungen in graphit”, *Zeitschrift für Physik A Hadrons and nuclei* **211**, 391–399 (1968).
- [76] R. Klucker, M. Skibowski, and W. Steinmann, “Anisotropy in the optical transitions from the π and σ valence bands of graphite”, *physica status solidi (b)* **65**, 703–710 (1974).
- [77] H. Venghaus, “Redetermination of the dielectric function of graphite”, *physica status solidi (b)* **71**, 609–614 (1975).
- [78] W. Olovsson, T. Mizoguchi, M. Magnuson, S. Kontur, O. Hellman, I. Tanaka, and C. Draxl, “Vibrational effects in x-ray absorption spectra of two-dimensional layered materials”, *The Journal of Physical Chemistry C* **123**, 9688–9692 (2019).
- [79] K. Chernenko, A. Kivimäki, R. Pärna, W. Wang, R. Sankari, M. Leandersson, H. Tarawneh, V. Pankratov, M. Kook, E. Kukk, L. Reisberg, S. Urpelainen, T. Käämbre, F. Siewert, G. Gwalt, A. Sokolov, S. Lemke, S. Alimov, J. Knedel, O. Kutz, T. Seliger, M. Valden, M. Hirsimäki, M. Kirm, and M. Huttula, “Performance and characterization of the FinEstBeAMS beamline at the MAX IV Laboratory”, *Journal of Synchrotron Radiation* **28**, 1620–1630 (2021).
- [80] F. J. Dyson, “The S matrix in quantum electrodynamics”, *Phys. Rev.* **75**, 1736–1755 (1949).
- [81] L. Hedin, “New method for calculating the one-particle green’s function with application to the electron-gas problem”, *Phys. Rev.* **139**, A796–A823 (1965).
- [82] G. Baym, “Self-consistent approximations in many-body systems”, *Phys. Rev.* **127**, 1391–1401 (1962).
- [83] D. Bohm and D. Pines, “A collective description of electron interactions. i. magnetic interactions”, *Phys. Rev.* **82**, 625–634 (1951).
- [84] D. Pines and D. Bohm, “A collective description of electron interactions: ii. collective vs individual particle aspects of the interactions”, *Phys. Rev.* **85**, 338–353 (1952).
- [85] D. Bohm and D. Pines, “A collective description of electron interactions: iii. coulomb interactions in a degenerate electron gas”, *Phys. Rev.* **92**, 609–625 (1953).
- [86] G. C. Wick, “The evaluation of the collision matrix”, *Phys. Rev.* **80**, 268–272 (1950).
- [87] J. Vinson, “Bethe-salpeter equation approach for calculations of x-ray spectra”, PhD thesis (University of Washington, 2012).

Humboldt-Universität zu Berlin
Mathematisch-Naturwissenschaftliche Fakultät
Institut für Physik

Name	Richter
Vorname	Elias
Matrikelnummer	588447

Selbstständigkeitserklärung

Ich erkläre hiermit, dass ich die vorliegende Arbeit mit dem Titel

*Time-Resolved Resonant Inelastic X-ray Scattering of Graphite from
First Principles*

selbstständig verfasst und noch nicht für andere Prüfungen eingereicht habe. Sämtliche Quellen einschließlich Internetquellen, die unverändert oder abgewandelt wiedergegeben werden, insbesondere Quellen für Texte, Grafiken, Tabellen, Bilder sowie die Nutzung von Künstlicher Intelligenz für die Erstellung von Texten und Abbildungen, sind als solche kenntlich gemacht. Mir ist bekannt, dass bei Verstößen gegen diese Grundsätze ein Verfahren wegen Täuschungsversuchs bzw. Täuschung eingeleitet wird.

Berlin, 21. Juli 2025



Elias Richter